

CRACK PATH SELECTION IN MICROSTRUCTURALLY TAILORED  
INHOMOGENEOUS POLYMERS

BY

JOSEPH FERNANDO GONZALEZ

THESIS

Submitted in partial fulfillment of the requirements  
for the degree of Master of Science in Aerospace Engineering  
in the Graduate College of the  
University of Illinois at Urbana-Champaign, 2011

Urbana, Illinois

Adviser:

Professor John Lambros

## Abstract

In this work, the wide range of properties of a photodegradable polymer are exploited to generate a host of different inhomogeneous arrangements that can help us experimentally study crack path selection problems. The model material which we are using is a polyethylene copolymer, ECO, whose photosensitive behavior allows alterations in its mechanical properties when subjected to ultraviolet (UV) irradiation. It is seen that ECO becomes stiffer but more brittle upon UV irradiation. Material degradation in such polymers enables their use as an environmentally friendly material that can be broken into smaller nontoxic parts under small forces such as wind and light. This model material is then used to generate microstructures that possess either discrete or distributed local inhomogeneities similar to granular materials, *i.e., metals*.

The first part of this literature describes the experimental work done on the three microstructures developed. The microstructures all exhibited the same grain properties but possessed varying grain boundary properties. Each microstructure was loaded in a single edge notch tension (SENT) configuration, and the resulting strain fields were recorded using digital image correlation (DIC). Depending on the applied load and the local microstructure, different crack paths occur, such as the main crack simply extending, or a main crack arresting and a host of secondary cracks appearing at critical locations. Additionally, different types of failure occur within the granular inhomogeneous model displaying intergranular and/or transgranular failure for specific hours of UV irradiation. The DIC results, correlated with global load-displacement measurements, shed light on the conditions under which local crack nucleation and growth can occur.

In the second part of this work, the global load-displacement results are compared with a finite element model using ABAQUS. Two different models, interface and interphase, are created to assist in validating the experimental results. Through comparison of the global load-displacement results with the experimental and numerical study, the different developed models can be seen to represent a particular microstructure. A failure criteria is also considered using numerical analysis by analyzing areas of high stress levels using the von Mises and Tresca yield criteria. These criteria illustrate areas in which high magnitudes of stress occur and these results are compared with the experimental failure initiation sites.

*To God for always giving me the strength and  
faith to overcome life's obstacles.*

## **Acknowledgements**

There are many people that have contributed in my success as a person and in this research. I would like to thank Professor John Lambros for taking me under his wing when I was at first an undergraduate researcher. Throughout the years, he has given me guidance and support to help me improve with my education and research. I really appreciate the mentoring he has provided in regards to my research and with life in general. One great thing that I admire is Professor Lambros' understanding and patience. I would also like to thank the Lambros' group: Owen Kingstedt, Mallory Casperson, Tommy On, Erheng Wang, Bharath Swaminathan, Peter Lavigne, and Robert Waymel. Special thanks to Owen for his humor and support throughout my graduate degree. I owe thanks to Alpay Oral for helping me with questions I had with the finite element program, ABAQUS.

I want to send a great deal of thanks to those closest to me including my family, best friends, and girlfriend. I thank my parents for raising me the right way, teaching me to always work hard, and pursue whatever my heart desired. I will never trade their love for anything and I hope to one day give my children the opportunities they have blessed me with. My brothers and sister, Anthony, Adrian, and Ainee, are always there to make me smile and keep me motivated. I enjoy all the video games, movies, and dinners that we have share together. I would like to give a "shout out" to my good friends who have been there for me through it all and have given nothing but good times, support, and brotherly love: Eric Elleby, Dimitrios Antartis, and Enrique Carrion. Lastly, I would like to thank my beautiful girlfriend, Taissa Bergeman, for coming into my life and providing me with unconditional love and support each and every day.

# Table of Contents

List of Figures .....	vii
List of Tables .....	x
Chapter 1: Introduction .....	1
1.1 Motivation and Background .....	1
1.2 Objectives of This Work.....	5
1.3 Thesis Outline .....	6
Chapter 2: Experimental Techniques .....	8
2.1 Material .....	8
2.2 Specimen Preparation .....	10
2.2.1 Uniaxial Tension Specimens.....	12
2.2.2 Granular Specimens .....	13
2.3 Experimental Setup.....	15
2.4 Digital Image Correlation .....	17
Chapter 3: Experimental Results .....	21
3.1 Polyethylene Tension Results.....	21
3.2 Granular Force Displacement Results .....	26
3.2.1 High Boundary Toughness - 1 Hr Irradiation .....	27
3.2.2 Medium Boundary Toughness - 10 Hr Irradiation.....	30
3.2.3 Low Boundary Toughness - 50 Hr Irradiation.....	33
3.3 Digital Image Correlation Results .....	36
3.3.1 High Boundary Toughness– 1 Hr Irradiation .....	37
3.3.2 Medium Boundary Toughness – 10 Hr Irradiation.....	41
3.3.3 Low Boundary Toughness – 50 Hr Irradiation .....	43
Chapter 4: Finite Element Analysis .....	45
4.1 Numerical Setup .....	45
4.1.1 Interface and Interphase Models .....	45
4.1.2 Material Property Allocation .....	47
4.1.3 Boundary Conditions .....	49
4.1.4 Mesh.....	50
4.2 Numerical Results.....	54
4.2.1 Interface Model .....	54
4.2.2 Interphase Model - High Boundary Toughness .....	55
4.2.3 Interphase Model - Medium Boundary Toughness.....	57
4.3 Failure Criteria.....	58
Chapter 5: Conclusions and Future Work .....	62
References .....	66

## List of Figures

<b>Figure 1.1</b> (Left) Contour plot of the residual fatigue-accumulated plastic strain $\epsilon_{yy}$ field – normal to the crack direction. (Right) Magnified portion of an area comparing the local microstructure from EBSD to the strain field from DIC (Carroll <i>et. al.</i> , 2010). ....	2
<b>Figure 1.2</b> The sample surface and the axial strain field at 50× magnification, and the approximate DIC subset size shown as a yellow filled square. The rightmost strain field is included to suggest the location of grain boundaries. (Refer to web version of paper for references to color in figure legend) (Efstathiou <i>et. al.</i> , 2010) .....	3
<b>Figure 1.3</b> Local strain analysis of A220 deformed incrementally with compression test (compression direction perpendicular to image plane). Both images show steps up to 60% total macroscopic strain and the grain microstructure is shown with black lines in the image. The strain field on the left shows $\epsilon_{xx}$ and image on the right shows $\epsilon_{xy}$ . (Rehrl <i>et. al.</i> , 2011) .....	4
<b>Figure 2.1</b> Stress-strain curves displaying the effects of increasing irradiation time on ECO (Abanto-Bueno and Lambros, 2004). ....	10
<b>Figure 2.2</b> Specimens for tension experiments (left) and a close up view of the speckle pattern from a sample tension specimen (right). ....	12
<b>Figure 2.3</b> Granular pattern template used for irradiation. Numbers indicated within the grains reveal hours of UV irradiation. ....	14
<b>Figure 2.4</b> Granular boundary of the UV irradiation pattern and the varying hours of irradiation with defined toughness. ....	14
<b>Figure 2.5</b> Experimental setup of equipment used to carry out experiments. MTS machine connects to Compaq computer to acquire data from TestWorks and the Sony camera connects to the HP computer for image storage. ....	17
<b>Figure 2.6</b> DIC technique for rigid body rotation of 30 with the subset compared in both images: a) undeformed b) deformed (Abanto-Bueno and Lambros, 2004). ....	18
<b>Figure 2.7</b> Scale of observation: subset size and subset size with a sample grid of pixels compared to grain sizes. ....	20
<b>Figure 3.1</b> (a) Stress-strain curves for varying hours of UV exposure and (b) stress-strain curves for varying hours of UV exposure with a smaller strain window less than 20%. The arrow shows that the failure stress increases and the material becomes brittle as exposure time increases. ....	22
<b>Figure 3.2</b> Average values of the Young's modulus as a function of UV irradiation time. ....	23
<b>Figure 3.3</b> Average values of failure stress as a function of UV irradiation time. ....	24
<b>Figure 3.4</b> Average values of failure strain as a function of UV irradiation. ....	24

<b>Figure 3.5</b> Measured force-displacement curves for the high (1 hr), medium (10 hr), and low (50 hr) toughness specimens with closer image of the polynomial fitted data marked with solid lines. .....	27
<b>Figure 3.6</b> Force-displacement response of the high boundary toughness specimen with blue boxed locations showing the real time images below the graph (pre failure denoted as P1 and P2, and additional locations after initial failure marked with A1, A2, <i>etc.</i> ) .....	29
<b>Figure 3.7</b> Occurrence of cracks of the high boundary toughness in the order of which they appear throughout the test on an image of the granular template (order of crack occurrences marked with shaded blue circle). .....	30
<b>Figure 3.8</b> Force-displacement response of the medium boundary toughness specimen with red boxed locations showing the real time images below the graph (pre failure denoted as P1 and P2, and additional locations after initial failure marked A1, A2, <i>etc.</i> ) .....	32
<b>Figure 3.9</b> Occurrence of cracks for the medium boundary toughness in the order of which they appear throughout the test on an image of the granular template (order of crack occurrences marked with shaded red circle). .....	33
<b>Figure 3.10</b> Force-displacement response of the low boundary toughness specimen with magenta boxed locations showing the real time images below the graph (pre failure denoted as P1, and additional locations after initial failure marked A1, A2, <i>etc.</i> ) .....	35
<b>Figure 3.11</b> Occurrence of cracks for the low boundary toughness specimen in the order of which they appear throughout the test on an image of the granular template (order of crack occurrences marked with shaded magenta circle). .....	36
<b>Figure 3.12</b> Force-displacement response of the high boundary toughness specimen in relation to DIC strain measurements, $\epsilon_{yy}$ , for displacements of: (a) 1.57 mm (b) 3.57 mm (c) 5.57 mm (d) 6.31 mm (e) 6.79 mm (f) 6.90 mm.....	39
<b>Figure 3.13</b> DIC measurements of (a) the shear strain, $\epsilon_{xy}$ , and the (b) x-direction strain, $\epsilon_{xx}$ , at crack initiation with 6.31 mm of displacement.....	40
<b>Figure 3.14</b> Force-displacement response of the medium boundary toughness specimen in relation to DIC strain measurements, $\epsilon_{yy}$ , for displacements of: (a) 1.31 mm (b) 4.31 mm (c) 6.53 mm (d) 6.87 mm (e) 7.58 mm (f) 9.31 mm.....	42
<b>Figure 3.15</b> Force-displacement response of the low boundary toughness specimen in relation to DIC strain measurements, $\epsilon_{yy}$ , for displacements of: (a) 3.1 mm (b) 5.1 mm (c) 6.1 mm (d) 6.6 mm (e) 6.9 mm (f) 7.1 mm. ....	44
<b>Figure 4.1</b> Interphase model used for finite element simulations. In this model, the grain boundaries show irradiation of 1 hr. Color key for each irradiation time can be seen to the right. .....	46



<b>Figure 4.2</b> Interface model used for simulation. In this model, the grain boundaries are excluded. The color key for the rest of the grains can be seen to the right. ....	46
<b>Figure 4.3</b> Interphase model showing applied boundary conditions. The entire bottom edge has $u_y = 0$ ; the bottom left corner also has $u_x = 0$ , and the entire top edge a $u_y$ specified displacement (in mm) as recorded from the experiments. ....	50
<b>Figure 4.4</b> Mesh convergence for varying average nodal displacements for interphase model. .	52
<b>Figure 4.5</b> Numerically simulated stress fields produced for 6 mm of displacement for varying meshes of different nodal distances: (a) 6 mm, (b) 5 mm, (c) 4 mm, (d) 3 mm, (e) 2 mm, and (f) 1 mm. These images were used as a mesh convergence test to choose which mesh to implement. ....	53
<b>Figure 4.6</b> Interface model with a thickness of 0.51 mm plotted against actual experiments. ....	55
<b>Figure 4.7</b> Interphase high boundary toughness simulations compared to actual. Simulation included low and high range of the material thickness (0.48 mm and 0.51 mm) and the boundary widths of 3 mm and 6 mm. ....	56
<b>Figure 4.8</b> Interphase high boundary toughness simulations with increasing thickness compared to actual. ....	57
<b>Figure 4.9</b> Interphase medium boundary toughness simulation compared to actual. Simulation included low and high range of the material thickness (0.48 mm and 0.51 mm) and the boundary widths of 3 mm and 6 mm. ....	58
<b>Figure 4.10</b> a) The order of crack initiation, shown by numbers, for the high boundary toughness experiment; b) Von Mises yield criterion displaying areas of high equivalent stress; c) Tresca max shear stress yield criterion displaying areas of high max stress. ....	60
<b>Figure 4.11</b> a) The order of crack initiation, shown by numbers, for the medium boundary toughness experiment; b) Von Mises yield criterion displaying areas of high equivalent stress; c) Tresca max shear stress yield criterion displaying areas of high max stress. ....	61

## List of Tables

<b>Table 4.1</b> Young's modulus and true yield stress values for different hours of irradiation used for numerical properties.....	48
---	----

# Chapter 1

## Introduction

### 1.1 Motivation and Background

Over the past decades, as multiscale mechanics has evolved, there has been increasing interest in correlating a material's microstructure with the development of its local strain fields, as this is believed to provide indications of the material response at the macroscale. Thus understanding the local response of material microstructures has become vital towards creating improved materials for applications that require increased protection, strength, and durability. Many research efforts in the area of microstructural strain analysis have involved granular materials such as metals and ceramics (Hoffman *et. al.*, 2001; Raabe *et. al.*, 2001; Bartali *et. al.*, 2009; Carroll *et. al.*, 2009; Carroll *et. al.*, 2010; Saai *et. al.*, 2010; Efstathiou *et. al.*, 2010; Rehrl *et. al.*, 2011). These granular materials appear homogeneous at the macroscale – length scales much larger than the grain size – but at the microscale they possess highly inhomogeneous microstructures.

In the past there have been several experimental techniques used to correlate material microstructures with the development of local strain fields, such as a combination of the optical technique of digital image correlation (DIC) and the microstructure analysis technique of electron backscatter diffraction (EBSD). DIC is a technique that produces full-field displacements and strain measurements by comparing a deformed image with a random speckle pattern applied on the surface to a reference, or undeformed, image. The DIC algorithm will not be described here in detail but more information on DIC can be found in Section 2.4, and in the works of Sutton *et. al.* (1983). EBSD is commonly used to produce microstructural images, or

orientation maps, of a specimen grain structure. Together, EBSD and DIC techniques can then be used to relate the development of strain fields within a granular microstructure. In a recent study by Carroll *et. al.* (2010), fatigue crack growth in a nickel based superalloy, Hastelloy X, was studied using the combination of EBSD and DIC techniques. An example is illustrated in Figure 1.1 and shows a high resolution DIC-measured strain field and the corresponding EBSD result of a close up of the material grain structure. Strain concentrations at specific grain boundaries are resolved.

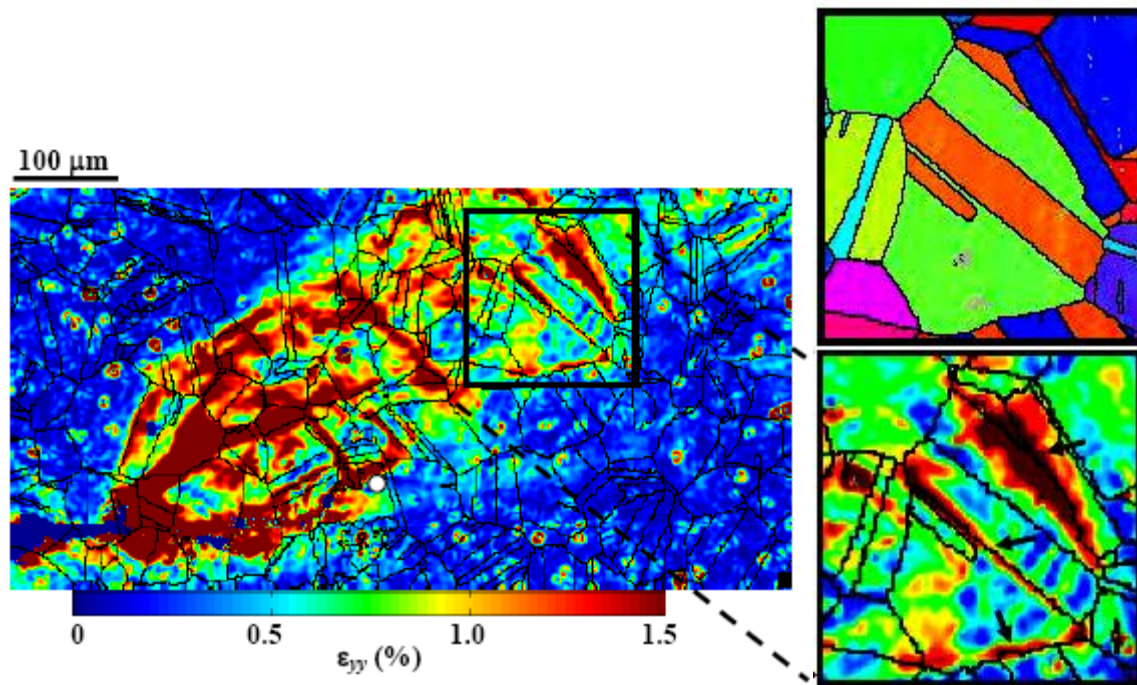


**Figure 1.1** (Left) Contour plot of the residual fatigue-accumulated plastic strain  $\epsilon_{yy}$  field – normal to the crack direction. (Right) Magnified portion of an area comparing the local microstructure from EBSD to the strain field from DIC (Carroll *et. al.*, 2010).

In another study done by Efstathiou *et. al.* (2010), the experimental technique of DIC was used to correlate the strain development with the microstructure of plastically deforming titanium. The spatial distribution of the deformation from uniaxial cyclic tensile loading was observed at various scales such as the mesoscale (a few grains) and the macroscale (hundreds of

grains). In this work, strain heterogeneities with grains were ascertained at 50× optical magnification. Figure 1.2 shows a surface image of the titanium material at 50× magnification (far left), the DIC-measured axial strain field (middle), and its comparison to the microstructure (far right).

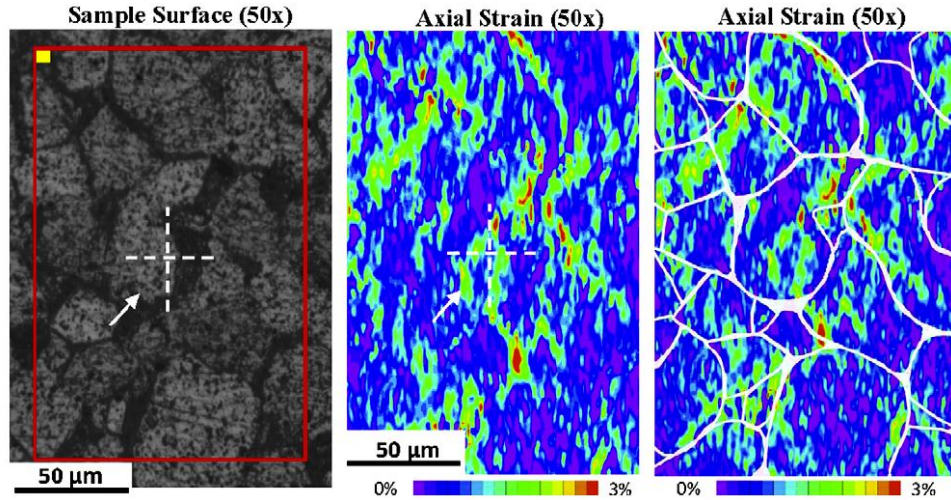


**Figure 1.2** The sample surface and the axial strain field at 50× magnification, and the approximate DIC subset size shown as a yellow filled square. The rightmost strain field is included to suggest the location of grain boundaries. (Refer to web version of paper for references to color in figure legend) (Efstathiou *et. al.*, 2010)

More recently in the work of Rehr *et. al.* (2011), austenitic stainless steel, grade A220, was used to measure the local in-plane strains and local crystal orientations for large plastic strains using a compression test. Measurements in this study were performed by DIC and EBSD to find local crystal orientation measurements to compare to the strain fields. Figure 1.3 shows an example comparison between the crystal microstructure and the local strain fields for both  $\epsilon_{xx}$  and  $\epsilon_{xy}$  at 60% of strain for the compression test.

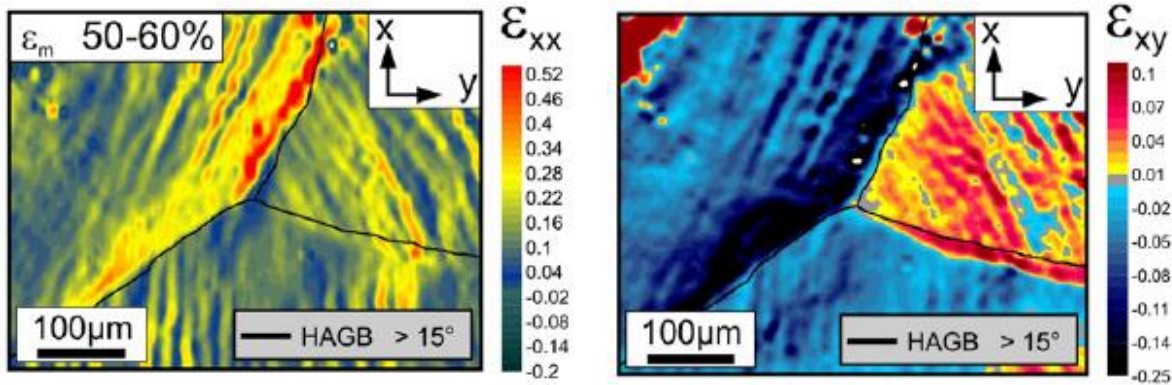


**Figure 1.3** Local strain analysis of A220 deformed incrementally with compression test (compression direction perpendicular to image plane). Both images show steps up to 60% total macroscopic strain and the grain microstructure is shown with black lines in the image. The strain field on the left shows  $\epsilon_{xx}$  and image on the right shows  $\epsilon_{xy}$ . (Rehrl *et. al.*, 2011)

Such previous research involving DIC and EBSD has shown great potential in relating strain field to microstructure, but there are still many uncertainties and questions about the methodology. DIC and EBSD are both surface measurements and involve two dimensional (2D) calculations. This fact brings attention to the question regarding the behavior and deformation evolution in the third direction, *i.e., the through-thickness direction*. Another uncertainty that complicates the use of results such as those shown in Figures 1.1-1.3 is the lack of knowledge of the local properties of each of the grains, and the grain *boundaries*, within the granular microstructure. Macroscale testing of ceramics and metals allows for the bulk properties of the material to be calculated, but determining properties at the microstructure is more complex. Methods like nanonindentation, single crystal experiments, *etc.*, have been used for this purpose (Liu *et. al.*, 2005; Liu *et. al.*, 2008; Lian *et. al.*, 2009; Gerday *et. al.*, 2011). However these experiments are complex to translate to the macroscale and often do not provide robust local elastic-plastic properties. Clearly, there is a lot of information that is obtained from such experimental techniques, but many aspects of the microstructure remain unknown.

## 1.2 Objectives of This Work

The main objective of this work is to address the limitations and unknowns in relating the local microstructure to the strain fields discussed above involving the combined use of the EBSD and DIC techniques (Bartali *et. al.*, 2009; Carroll *et. al.*, 2009; Carroll *et. al.*, 2010; Field *et. al.*, 2010; Saai *et. al.*, 2010; Efstathiou *et. al.*, 2010; Rehrl *et. al.*, 2011). Because of the lack of knowledge of the local and boundary properties of granular materials, we will conduct a series of experiments using a model “granular” material with highly controllable microstructure that will allow the development of well-controlled grain distributions with known *grain and grain boundary* properties. The microstructures will be geometrically similar to those appearing in the work of Carroll *et. al.* (2010) in which a granular pattern is used. The model material used is based on a polyethylene co-polymer that is highly sensitive to ultraviolet (UV) irradiation (Abanto-Bueno and Lambros, 2004); it is described in more detail in Section 2.1. In the setup employed in this work, the model material will be tailored to allow the development of intergranular failure at the grain boundaries and/or transgranular failure within the grains. Thus this material will address the lack of knowledge of local properties. We will exploit the material tailorability further by using very thin specimens which will both ensure uniformity of UV irradiation through the thickness and will bypass the issue of the evolution of failure in the third direction. Although perhaps not as directly relevant to thick structures, at least in our experiments the combination of microstructural information and strain evolution will not be influenced by subsurface phenomena. Finally, a common way of corroborating experimental results is through the technique of finite element analysis (FEA). A finite element model for each kind of experiment performed here will be developed in hopes of identifying an appropriate failure criterion to aid in the future tailoring of the model material.

In summary, the specific objectives of this work are to:

- (i) Study the mechanical response of well controlled microstructures where information regarding the local properties and boundary strengths are known *a priori*;
- (ii) Tailor the model material to produce different failure modes which will assist in understanding/controlling crack path development at the microscale;
- (iii) Develop finite element based numerical models which will correlate with experimental results regarding failure location and can assist in predicting failure in future tailored materials.

### **1.3 Thesis Outline**

The efforts in this thesis report experimentation on a highly tailorable polymeric material that will be used to achieve the objectives listed above. Chapter 2 describes the model material itself and how it is employed in this study to produce grain-like microstructures. For this purpose, the model material and fabrication parameters are based on the work of Abanto-Bueno and Lambros (2004). DIC is used to measure local strain levels, while macroscale response is determined through global force-displacement measurements. The DIC technique, along with the various other experimental details, is discussed in Chapter 2. Chapter 3 discusses the mechanical properties of the model material for different amounts of UV exposure and the results are compared with previous works. Chapter 3 also reveals the experimental results for three different granular specimens of the same microstructure but with different grain boundary strengths. Chapter 4 details the numerical model developed and reveals the results for each case of differing boundary strengths. The von Mises and Tresca failure criteria are also discussed in



analyzing the results and comparing against crack initiation. Chapter 5 provides the conclusions drawn from the overall research effort.

## Chapter 2

### Experimental Techniques

#### 2.1 Material

In order to study the mechanical response of well controlled microstructures, polyethylene carbon monoxide, referred to as ECO, will be utilized as a model material to assist in analyzing the stress distributions in inhomogeneous granular media. ECO is a photosensitive ductile co-polymer that is most commonly used in packaging, *i.e., plastic bags, food packaging, six pack soda rings, etc.* It is also a photodegradable material whose mechanical response can be altered by wavelengths from sunlight, visible light, and most severely, UV light. ECO is a semi-crystalline co-polymer that is in fact considered an enhanced degradable polymer in which exposure to UV light accelerates its mechanical degradation (Andrady, 1990). The photodegradable nature of ECO is enhanced by the addition of small amounts of photosensitive carbonyl groups [carbon monoxide (CO) ketones] to the backbone chain of low-density polyethylene, and results in a polyketonic structure  $[-(\text{CH}_2\text{CH}_2)_n-(\text{CO})_x-]$  where  $n$  and  $x$  depend on the specific molecular content (Abanto-Bueno and Lambros, 2004). In the present study, ECO containing 1 % wt.-carbon monoxide was used. Following the work of Lambros *et al.* (1999), Li *et al.* (2000), and Abanto-Bueno and Lambros (2004), hours of ECO exposure to UV irradiation are varied to alter the mechanical properties in a controllable fashion.

The changes within ECO's chemical and physical properties and structures are well understood (Trozzolo and Winslow, 1968; Hartley and Guillet, 1968; Heskins and Guillet, 1970; Li and Guillet, 1980; Torikai *et al.*, 1986; Nakatsuka and Andrady, 1994). The effect of UV light irradiation based on the thickness of ECO was studied by Furneaux *et al.* (1981). From

Furneaux's investigation, it was shown that sheets of irradiated low-density polyethylene (LDPE) with thicknesses of 0.8 mm or smaller will undergo uniform irradiation through the material thickness. In our work we use ECO sheets with a thickness ranging from 0.48 mm-0.51 mm. In addition to ensuring uniform irradiation, and thus mechanical properties, such a thin sheet assists us in studying the stress distributions generated since the stress state is simplified from a three-dimensional (3D) to a two-dimensional (2D) plane stress condition.

The low density polyethylene material was obtained from Hi-Cone, a division of Illinois Tools Works Inc., which also supplied the material for the studies of Lambros *et. al.* (1999), Li *et. al.* (2000), and Abanto-Bueno and Lambros (2004). The material used in this investigation was acquired in 2003 and was used in the investigation of Abanto-Bueno and Lambros (2004). Through the studies of Lambros *et. al.* (1999) and Abanto-Bueno and Lambros (2004), it was determined that UV light exposure time varies the mechanical properties of ECO, which becomes more brittle as UV irradiation time increases. Figure 2.1 shows uniaxial stress-strain curves from Abanto-Bueno and Lambros (2004) for ECO that was irradiated for varying hours. The unirradiated ECO specimen of 0 hrs shows very ductile behavior and has a failure strain of ~900 % (testing was stopped at a strain of 360 % in this case). However, as the hours of UV exposure increase, failure strain decreases and the elastic modulus and yield stress increase, as seen in the inset of Figure 2.1.

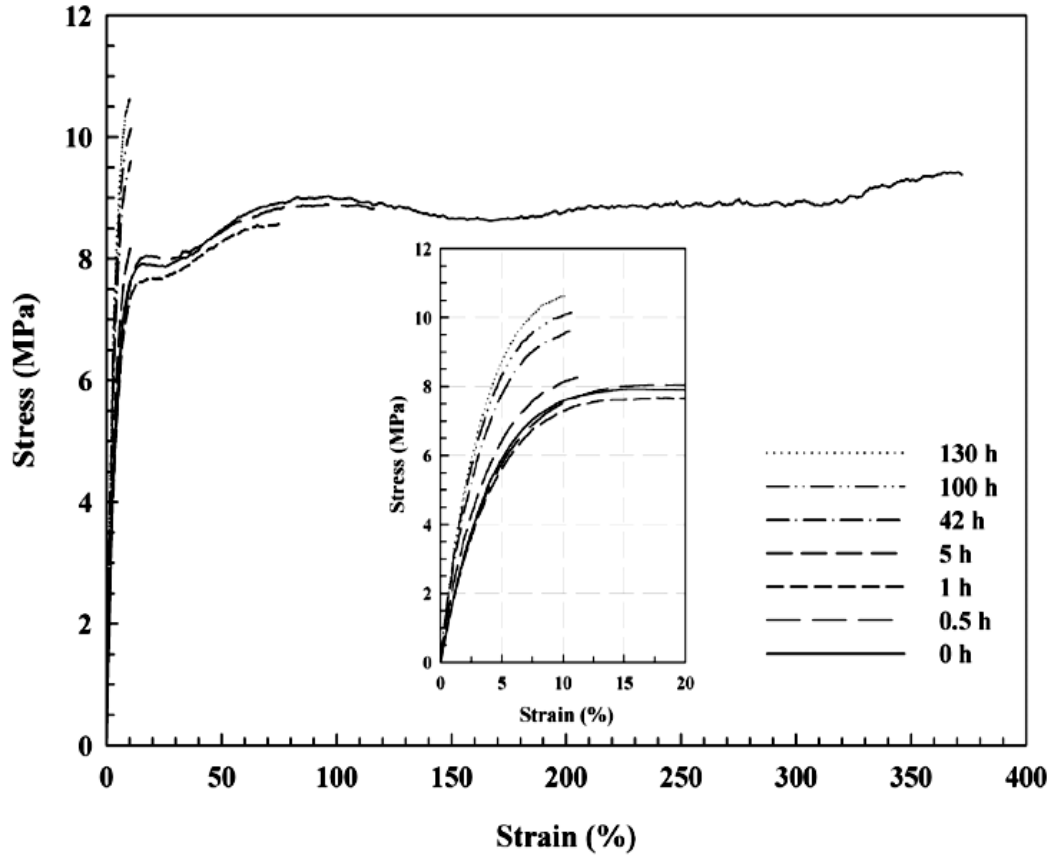


**Figure 2.1** Stress-strain curves displaying the effects of increasing irradiation time on ECO (Abanto-Bueno and Lambros, 2004).

## 2.2 Specimen Preparation

Although the ECO used here was stored for a period of years in a dry, dark and cool area, it may still have undergone some amount of degradation. Because of this risk, we cannot directly use the results of Abanto-Bueno and Lambros (2004) to design the inhomogeneous structures in this work using the properties of Figure 2.1. Consequently, the experiments performed by Lambros *et. al.* (1999), Li *et. al.* (2000), and Abanto-Bueno and Lambros (2004) were replicated to assist in understanding the mechanical behavior of the particular ECO used here. The first step in replicating these experiments started with the specimen fabrication. The unirradiated ECO

was cut into dimensions for each appropriate testing scheme – tension and granular tension, using an X-ACTO blade and cutting mat. Irradiation was done using a Cole-Palmer dual ultraviolet fluorescent table (Cole-Palmer Instrument Co., Vernon Hills, IL) after the material was cut into the appropriate dimensions for the different experiments. This table utilizes six fluorescent tubes that emit UV light at a wavelength of 254 nm, which is in the appropriate range for optimal (fastest) degradation of ECO (Andrady *et al.*, 1996). Since the UV fluorescent tubes have an estimated lifetime of 1,000 hrs, the six tubes were replaced after every seven hundred hours of irradiation in order to keep a consistent intensity of irradiation for all samples. The bulbs were replaced twice throughout the duration of this study, so the intensity can be assumed to be uniform throughout the irradiation processes.

Specimen grips similar to those used in the work of Abanto-Bueno and Lambros (2004) helped prevent slipping and kept the specimen stationary while in the load frame. The specimen grips were made out of sandpaper and cardboard and were joined with hot glue and staples. When the irradiation pattern was completed, the specimen was placed in a refrigerator (45°F) until testing in order to assist in controlling any thermal or moisture effects. Particles of drierite® (anhydrous calcium sulfate) were used maintain a dry atmosphere inside the refrigerator (Abanto-Bueno and Lambros, 2004). Before testing, the specimen was removed and allowed to cool to room temperature in a dark environment.

In order to measure *in situ* full-field strain, the optical technique of DIC was used (Sutton *et. al.*, 1983). This technique requires a random speckle pattern to be applied on the surface of the material. Black spray paint was employed to achieve this pattern, and was applied by using linear strokes along the horizontal of the specimen. Once the specimen was covered with one light coat, it was left to dry for a few minutes and then another coat was applied using the same

technique. The spray can was held about 7 inches away from the specimen during the application of the speckle pattern. Details of the DIC portion of the experiment are given in Section 2.4. Finally, the ends of the material specimen were stapled between two sandpaper grips, and then attached to the machine for testing (described in Section 2.3). More details regarding the tension and granular tension specimens are further discussed in the next sections.

### ***2.2.1 Uniaxial Tension Specimens***

In the specimen fabrication of the uniaxial tension specimens, the unirradiated ECO was first cut into dimensions of 150 mm  $\times$  10 mm for the tension tests. After the UV exposure was applied to the material, specimen grips were made for the tension specimens. The grips measured out at 25 mm  $\times$  25 mm and were stapled to the top and bottom of the specimens. Figure 2.2 displays the complete tension specimen with the applied speckle pattern, and the specimen grips. An enhanced view of the applied speckle pattern is provided for clarity.

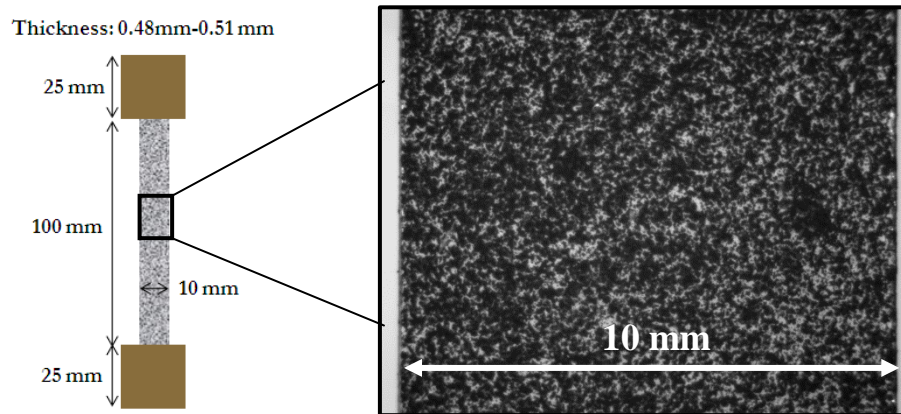


**Figure 2.2** Specimens for tension experiments (left) and a close up view of the speckle pattern from a sample tension specimen (right).

### ***2.2.2 Granular Specimens***

In the specimen fabrication of the granular specimens, the unirradiated ECO was cut into dimensions of 150 mm  $\times$  150 mm. The specimen grips differed in comparison to the simple tension specimens due to the fact that different machine grips were used for the granular tension tests. The sandpaper grips were cut into dimensions of 150 mm  $\times$  25 mm. Once assembled with the hot glue gun, holes were punched out of the granular specimen grips to accommodate for larger machine grips and the screws that are used to attach the grips. The left side of Figure 2.3 shows the final specimen fabrication, including grips and speckle pattern.

The granular specimens with UV exposure do not exhibit a uniform pattern like the tension specimens because the goal of this effort is to study the role of local and grain boundary inhomogeneities in the development and evolution of inhomogeneous material failure. For this purpose, samples possessing an inhomogeneous “grain” pattern were developed by selective UV irradiation and appropriate masking. The irradiation pattern was achieved by varying irradiation exposures for certain parts of the material, including the regions corresponding to the granular boundaries. The right side of Figure 2.3 shows the random granular pattern, which involves grains and the grain boundaries. The irradiation time of each granular region is denoted by the number within each grain. The granular template works as a puzzle in which all the individual grains and the boundary pieces can be placed on top of an ECO sheet during irradiation. By placing and removing the required pieces, the irradiation pattern shown in Figure 2.3 can be obtained. The grains were irradiated for UV exposure times of 0 hr, 1 hr, 2 hr, 5 hr, and 10 hr as shown in Figure 2.3. The grains’ (randomly chosen) irradiation exposure time was the same for all samples tested here, but the grain boundary areas were irradiated by either 1 hr, 10 hr, or 50 hr, to produce differing amounts of grain boundary strength (toughness) – and tougher – grain

boundary. These three cases will be labeled as the high, medium, and low boundary toughness experiments, respectively. Figure 2.4 shows the grain boundary piece (blue), which covers the areas between the grains that were irradiated for three different cases.

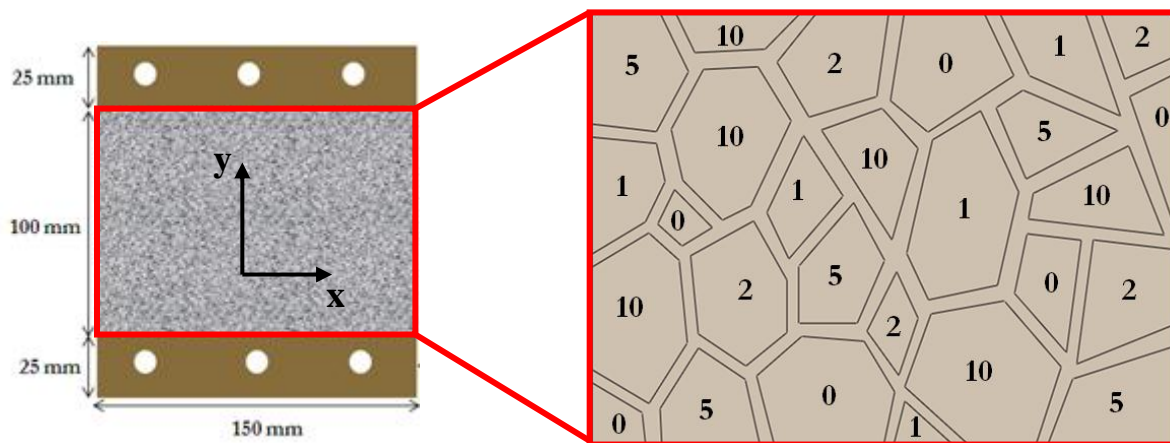
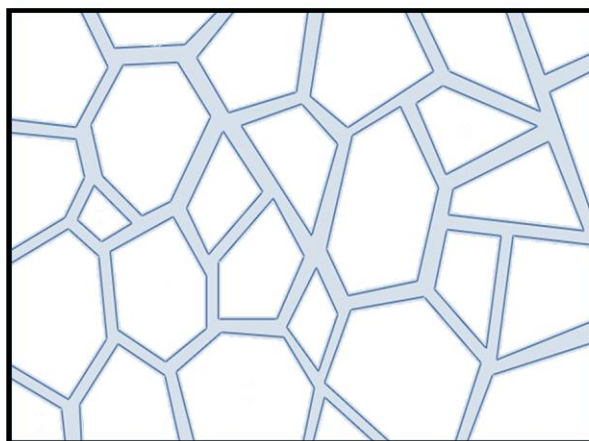


**Figure 2.3** Granular pattern template used for irradiation. Numbers indicated within the grains reveal hours of UV irradiation.



Boundary Irradiation Time (Hrs)	Toughness
1	High
10	Medium
50	Low

**Figure 2.4** Granular boundary of the UV irradiation pattern and the varying hours of irradiation with defined toughness.



This type of grain structure is meant to simulate that of polycrystalline metallic materials. However, unlike the case of such materials, in this work we precisely control the material properties (both elasto-plastic and toughness) of both the grain and the grain boundary regions. Knowing the precise values of local properties will facilitate an in-depth understanding of the significance of material heterogeneity on failure evolution. In addition, it will allow for a detailed numerical simulation of the exact geometry and properties used in the experiments.

### **2.3 Experimental Setup**

The machine used to perform the uniaxial tension tests was the screw driven MTS RT/30 tabletop universal testing machine (MTS Systems Corp., Eden Prairie, MN), which uses displacement control conditions. All experiments in this study were done with a constant crosshead speed of 0.5 mm/min, consistent with the work of Abanto-Bueno and Lambros (2004). The load cells were varied for each test; the uniaxial tension experiments used a 100 lb load cell (Transducer Techniques Inc., Temecula, CA), while the granular experiments used a 200 lb load cell (Lebow Products, Troy, MI). To control the MTS testing machine and acquire the crosshead displacement, load, strain, and stress at any given time, the universal testing software package TestWorks 4 ® (MTS Systems Corp., Eden Prairie, MN) was used on a Compaq desktop computer. Before the start of each test for the granular experiments, a pre-load was applied until the material was flat. This was done in order to assist with the DIC technique by allowing a flat plane reference image to be initially taken. Once testing began, each of the experiments was tested until material failure occurred.

For uniaxial tension experiments only, boundary loads were recorded and subsequently converted to stress and strain in the sample. Homogeneous uniaxial conditions were assumed

throughout, and successful experiments were considered those that failed away from the grip area. Throughout the duration of the granular experiments, images were taken automatically using a Sony IEEE 1394 digital CCD (model XCD-SC900,  $1280 \times 960$  pixels resolution) and Labview control software. The frame rate for picture acquisition was determined by the fastest speed at which the computer can obtain the pictures. A setting of 1 frame/s was used for the high toughness granular test, and a setting of 1/3 frames/s was used for the medium and low toughness granular tests. The initial laptop that was used for recording stopped working mid-experimentation, so a new HP desktop was used but had a slower picture acquisition rate due to a slower FireWire connection. The images were stored directly onto a separate computer from that controlling the load frame – namely a laptop/HP desktop computer using a FireWire interface. The images collected were subsequently used for obtaining DIC measurements (see Section 2.4). The data from the MTS machine stored in the Compaq desktop were later transferred to the HP desktop for analysis using Microsoft Excel and Matlab. The synchronization between the two different computers, *i.e.*, *pushing the start button on the HP desktop to begin picture storage and pushing start on the Compaq computer to begin testing*, was done manually. The reaction time for testing or picture acquisition to begin by pressing the start button is almost instantaneous and can be assumed to be much less than 1 second if pressed at the same time. This is completely dependent on human response but it can be assumed that acquisition occurred instantly for all experiments. Figure 2.5 shows a photograph of the setup and computer connections used for these experiments.

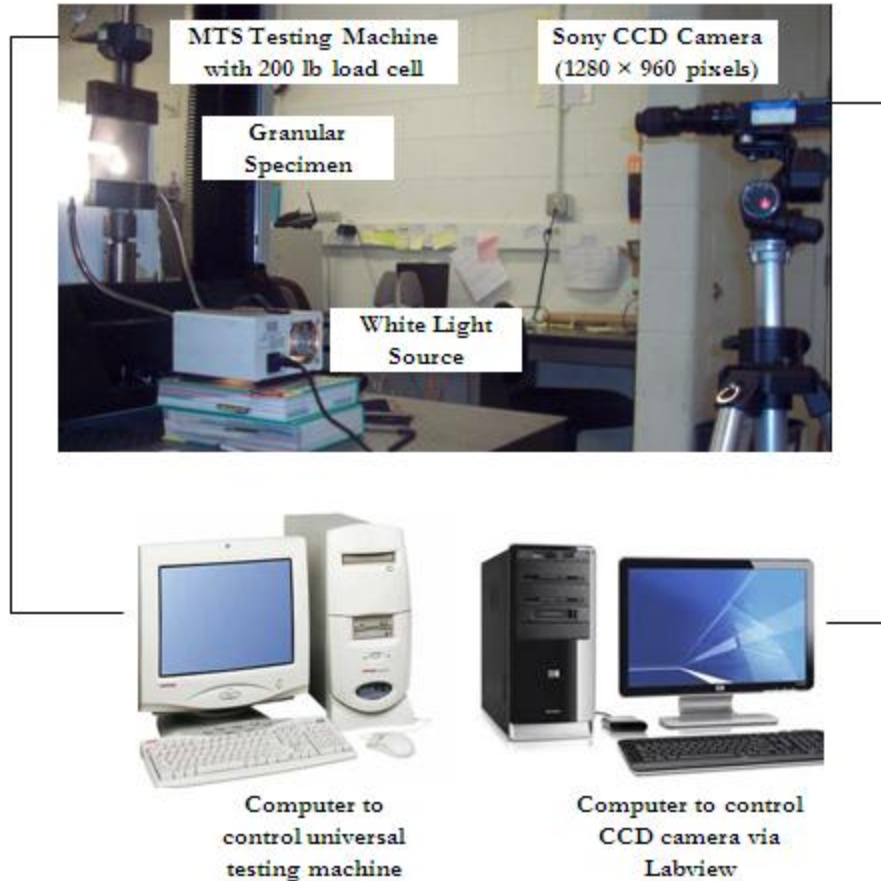


**Figure 2.5** Experimental setup of equipment used to carry out experiments. MTS machine connects to Compaq computer to acquire data from TestWorks and the Sony camera connects to the HP computer for image storage.

## 2.4 Digital Image Correlation

Many optical techniques have been used in solid mechanics to assist in measuring the strain and displacement fields of a material. One of the most commonly used optical techniques is that of DIC. DIC was developed in the early 1980s at the University of South Carolina and was used to measure the full-field in-plane displacements and strains of a deformed body (Peters and Ranson, 1982; Sutton *et. al.*, 1983; Peters *et. al.*, 1983; Chu *et. al.*, 1985). The DIC technique has many advantages over other optical methods; one important advantage is the

simplicity of the DIC setup. The only equipment needed for DIC is a computer, light source, and a digital CCD camera; the setup can be seen above in Figure 2.5.

The two dimensional DIC technique measures surface displacements and strains, *i.e.*,  $u_x$ ,  $u_y$ ,  $\partial u_x/\partial x$ ,  $\partial u_y/\partial y$ ,  $\partial u_x/\partial y$ , and  $\partial u_y/\partial x$ , by comparing a pair of images before and after deformation. After the pre-load was applied for each experiment, a reference image was taken before the start of the test and then images were taken throughout material testing (*i.e.*, *the deformed images*). DIC requires that a distinct and random speckle pattern be visible on the material in order to achieve the digital comparison of images. The randomly speckled pattern on the surface can be produced either naturally (*e.g.*, *roughness*) or artificially (*e.g.*, *paint*).

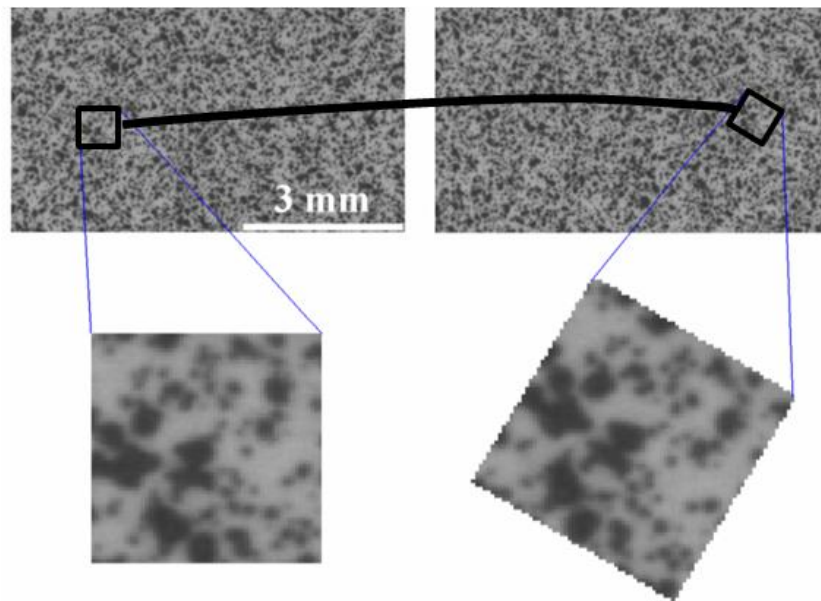


**Figure 2.6** DIC technique for rigid body rotation of 30 with the subset compared in both images: a) undeformed b) deformed (Abanto-Bueno and Lambros, 2004).

The measurements are done by matching small regions of the image, also called subsets, between the undeformed image, or reference image, and the deformed one. Figure 2.6 shows an illustration of subset matching in the DIC technique for a rigid body rotation in which a subset

size is defined and compared between the undeformed and deformed image. The details of how the correlation is done will not be given here in the interest of brevity. The reader is referred to Sutton *et. al.* (1983) for more details.

One of the most important aspects in DIC is defining the subset size, since this effectively represents the gauge length over which displacement and strain measurements will be made. As mentioned earlier, DIC compares (or correlates) the subsets throughout an undeformed image with a deformed image and produces an average value of surface displacements and strain fields over the subset. If a large subset size is used, the DIC technique results in a more non-local measurement, and consequently, less sensitive displacement and strain gradients (specifically, they are underestimated). If a smaller subset is used, the DIC technique, although providing a more local measurement, will be less able to converge to a correlated value. Thus, generally it is advisable to use the smallest subset size that still allows sufficiently accurate correlation between reference and deformed images (Carroll *et. al.*, 2009). These values, however, will depend on the pattern used.

In the present work, the speckled pattern for DIC was achieved by using black spray paint (refer to Section 2.2). The typical settings used during image correlation were a subset size of 51x51 pixels and a step size of 5 pixels between correlation points (*i.e., the center points of the subset*). Since we are interested in observing strain localization (*i.e., large strain gradients*) in a granular medium, the relative ratio of subset size to grain size will control how well we can resolve gradients at a sub-grain level (Carroll *et. al.*, 2009). Figure 2.7 shows the subset and step sizes used in this work in relation to the grain and grain boundary sizes within the material manufactured. The subset size has to be large enough to ensure that there is a sufficiently distinctive pattern contained in the area used for correlation.

The granular pattern, including the boundary regions, is outlined in the image of Figure 2.7 and the painted speckle pattern is also visible throughout. In each experiment the dimension and pattern were the same, so the same DIC parameters were used in the correlation. With these parameters, multiple subsets can be seen to fit within an average grain. The correlation yielded an average of 360 correlation points within a grain (assuming  $120 \text{ pixel} \times 120 \text{ pixel}$  grain sizes with subset size of 51 and step size of 5). These have been seen to be sufficient for sub-grain resolution measurements (Carroll *et. al.*, 2009).

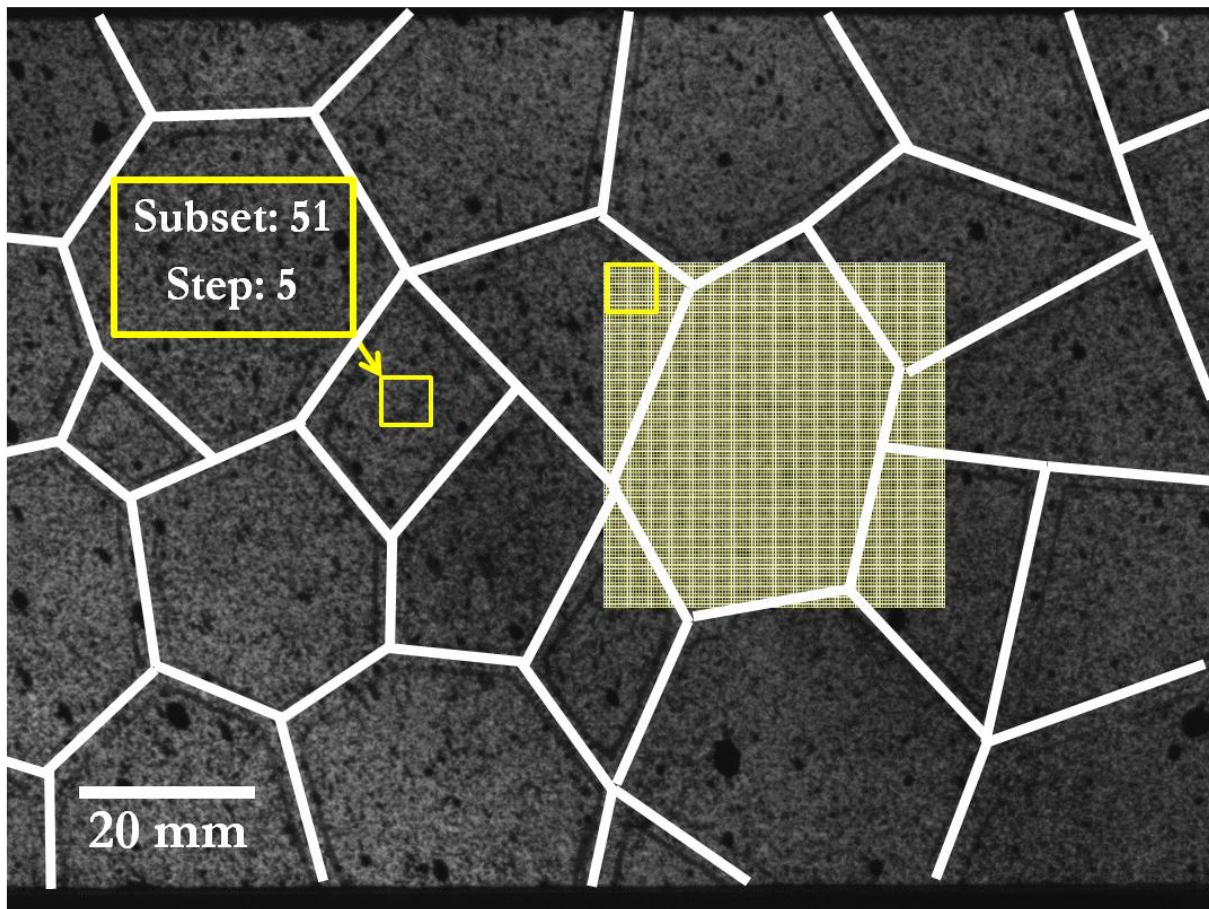


**Figure 2.7** Scale of observation: subset size and subset size with a sample grid of pixels compared to grain sizes.

## Chapter 3

### Experimental Results

#### 3.1 Polyethylene Tension Results

The first set of experiments that were carried out were the ECO uniaxial tension tests for varying hours of irradiation. A collection of stress-strain curves obtained for different hours of irradiation can be seen in Figure 3.1. The uniaxial tension tests were done in order to identify any differences from the material used in Abanto-Bueno and Lambros (2004) which is nominally the same as that used here. In Figure 3.1(a), the stress-strain curves display the overall mechanical behavior with a window of 250 % failure strain. The unirradiated ECO reached failure strains in excess of 250 %. While the failure strain of unirradiated ECO varied between 900 % and 360 % in previous works (Lambros *et. al.*, 1999; Abanto-Bueno and Lambros, 2004), the current unirradiated ECO failure strain reached a maximum value of about 500 %. There was significant material scatter, perhaps more so in this case since the material used was in storage for several years, therefore the uniaxial stress-strain curves shown in Figure 3.1 are the curves that represent the closest test to average based on the high and low range of data taken. Tension testing results were compared between three to five tension tests per each hour of UV irradiation and the test that represented the average most closely was chosen.

As mentioned in the previous section, each test performed was done under a controlled displacement of 0.5 mm/min. To better visualize the mechanical property changes that occur with increasing UV exposure time, a smaller strain region has been plotted in Figure 3.1(b). From Figure 3.1(a) and (b), it can clearly be seen that, in general, the elastic modulus increases, the failure stress increases, and failure strain decreases with increasing irradiation time, thus

embrittling the material. This observation is similar to that in the work from Abanto-Bueno and Lambros (2004).

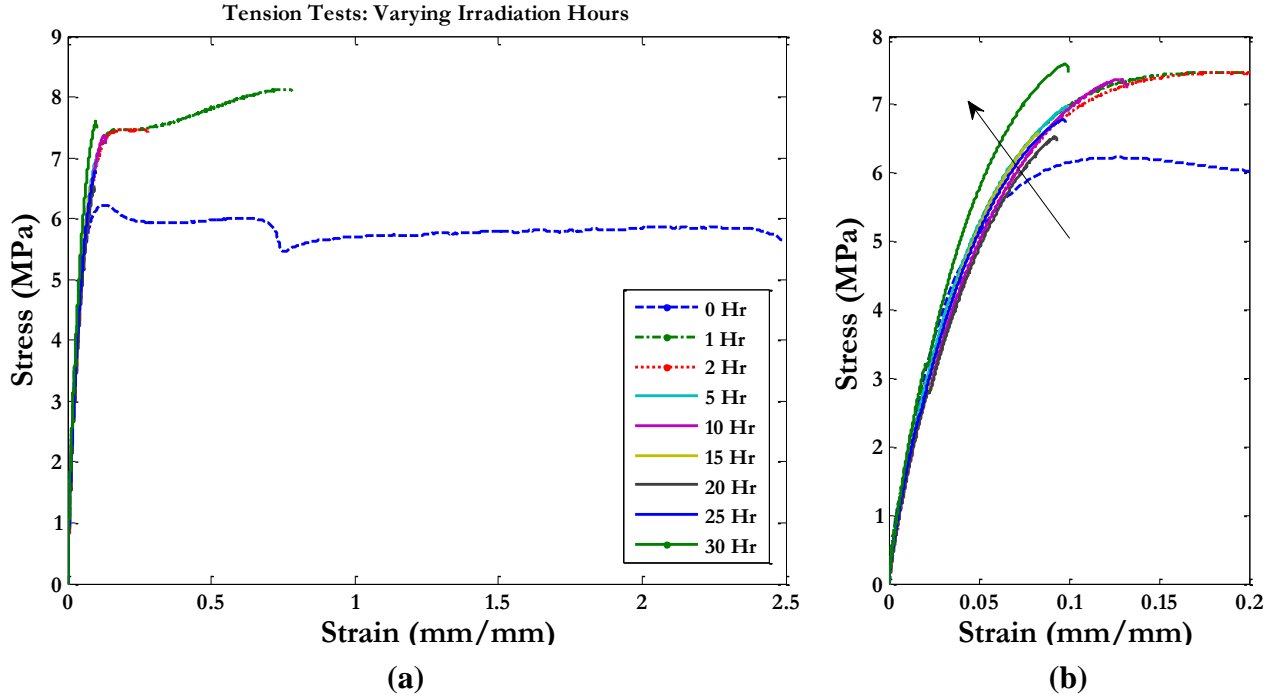


**Figure 3.1** (a) Stress-strain curves for varying hours of UV exposure and (b) stress-strain curves for varying hours of UV exposure with a smaller strain window less than 20%. The arrow shows that the failure stress increases and the material becomes brittle as exposure time increases.

The typical values of Young's modulus, failure strain, and failure stress are presented in Figures 3.2, 3.3, and 3.4 as a function of irradiation time. Each figure is plotted with scatter bars that graphically represent the spread from the high and low values from the individual experiments for each varying UV exposure time. In Figure 3.2 it is easy to discern that the Young's modulus values increase proportionally with the hours of UV irradiation. The majority of the tests for this particular study were consistent as the scatter per each set of tests was small. The average failure stress, Figure 3.3, shows similar behavior to that of the Young's modulus as the failure stress increases with an increase in UV exposure time; however, the scatter in the



average failure stress for each of the hours of irradiation is more pronounced, especially in the early hours of irradiation. In Figure 3.4, we see that the failure strain decreases with increasing hours of irradiation and eventually levels out at ~10% for hours of irradiation exceeding 5 hrs. As for the case of the failure stress, the scatter is high during the early times of UV exposure but becomes quite diminished for UV exposure greater than 5 hrs. From Figures 3.1-3.4, it is apparent that UV light exposure alters the mechanical response of ECO in a fashion very similar to that seen in previous works (Andrady, 1990; Andrady *et al.*, 1993; Li *et al.*, 1993; Ivanova *et al.*, 1996; Andrady *et al.*, 1996; Lambros *et al.*, 1999; Li *et al.*, 2000; Abanto-Bueno and Lambros, 2004).

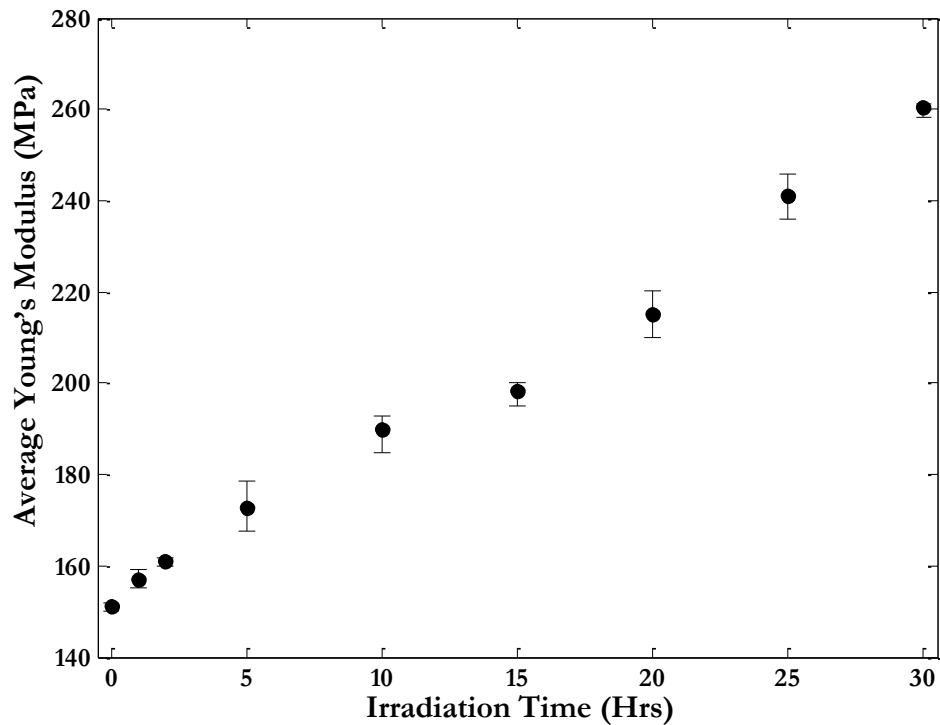


**Figure 3.2** Average values of the Young's modulus as a function of UV irradiation time.

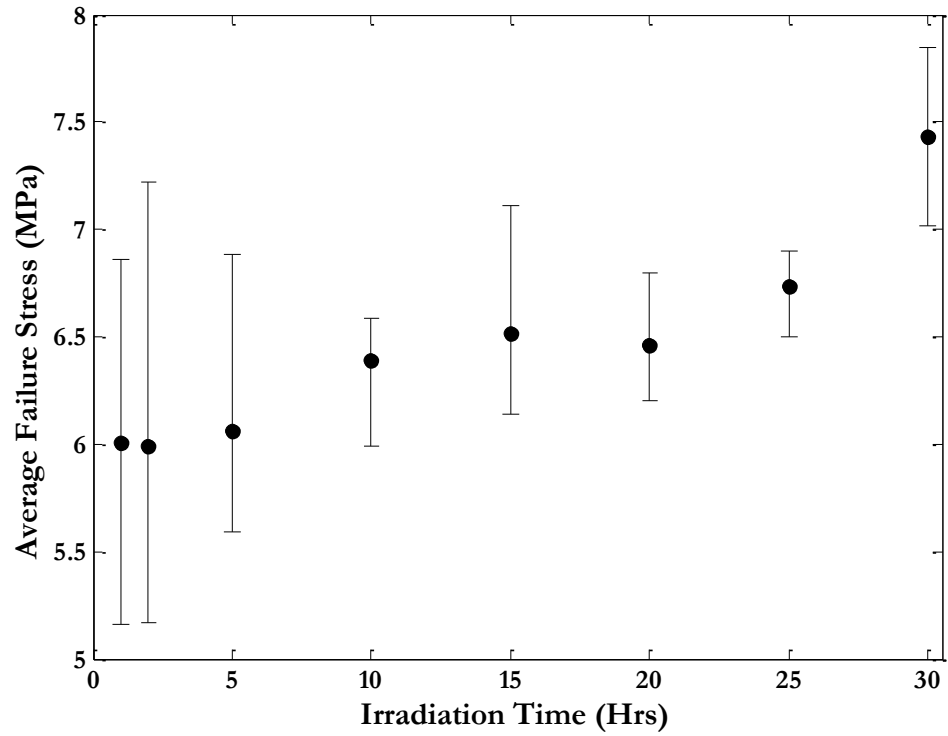


**Figure 3.3** Average values of failure stress as a function of UV irradiation time.

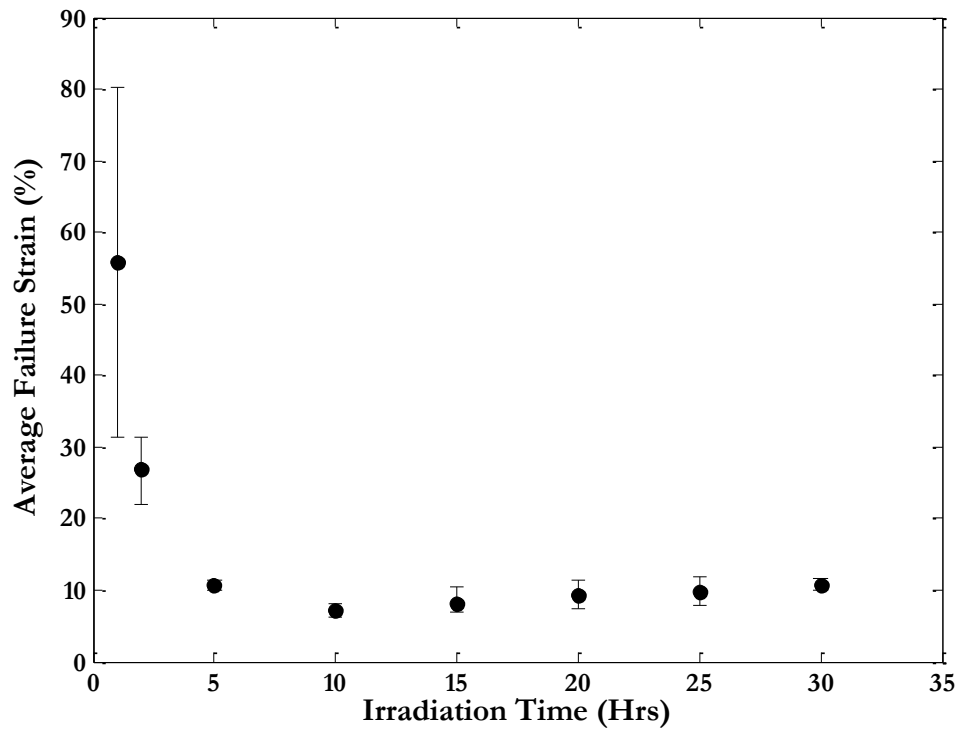


**Figure 3.4** Average values of failure strain as a function of UV irradiation

One difference in comparing the present results with past results, such as those of Abanto-Bueno and Lambros (2004) shown in Figure 2.1, is in the measured values of Young's modulus and failure stress. The present results show values for both the Young's modulus and failure stress lower than the past results, ~16 % and ~26 % respectively (Abanto-Bueno and Lambros, 2004). However, the failure strain displayed almost identical results when comparing both studies. The explanation for such discrepancies is likely that the material used here, although identical to that of Abanto-Bueno and Lambros (2004), has been in storage for some years. Even though the storage was in a cool, dark, and dry place, some material degradation may have occurred. Nonetheless, for the state of the material used here we have demonstrated that ECO becomes more brittle, stiffer, and stronger with increasing UV exposure time.

### 3.2 Granular Force Displacement Results

The model 2D granular specimens were also tested in uniaxial tension. Three types of granular specimens, differing only by boundary irradiation times, were used. As mentioned in Section 2.2.2, 1 hr, 10 hr, and 50 hr grain boundaries were manufactured and were identified as high, medium, and low boundary toughness experiments, respectively. For each experiment, the applied load was recorded and plotted as a force-displacement curve. As mentioned in Section 2.3, a small preload was applied in each case before the experiment started. Therefore the force data in each case were shifted to compensate for this (known) amount. A polynomial (5<sup>th</sup> order) fit, was used as a means of shifting the curves in each case, and is seen as a solid black line for each test in Figure 3.5, which shows typical measured applied force-displacement curves for the high, medium, and low toughness specimens. The high boundary toughness strength resulted in the highest maximum force (524.6 N); however, the medium toughness experiment had maximum force of 451.4 N, while the low toughness experiment had a maximum force of 470.8 N – higher than that of the medium toughness. This result might be attributed to material variability, which is considerable for irradiation times below 5 hr. Another intriguing result is the behavior of each experiment associated with the load drops after the main peak; the force-displacement curve drops rapidly for the high toughness experiment but has a more gradual drop for both the medium and low toughness experiments. This suggests a different failure evolution sequence in each case, and will be examined more closely in the following subsections with the aid of the real time images and DIC analysis performed in each case.

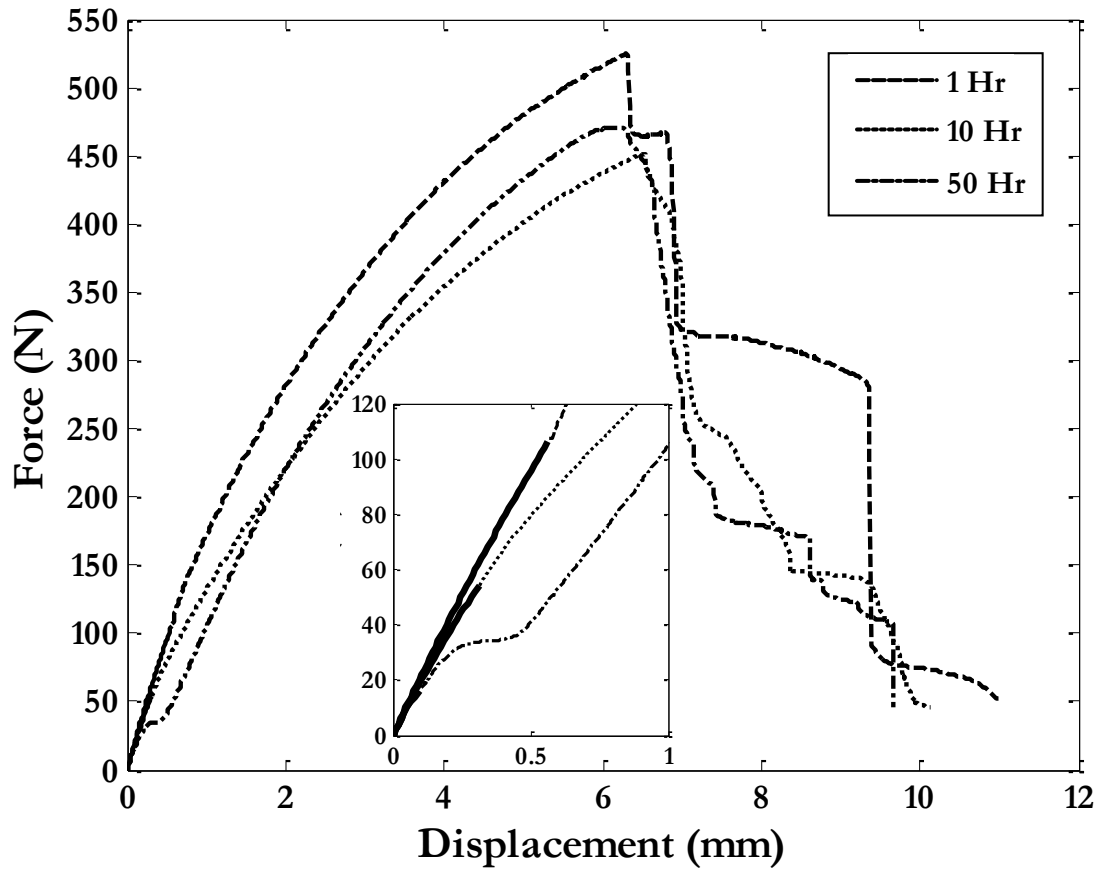


**Figure 3.5** Measured force-displacement curves for the high (1 hr), medium (10 hr), and low (50 hr) toughness specimens with closer image of the polynomial fitted data marked with solid lines.

### 3.2.1 High Boundary Toughness - 1 Hr Irradiation

The high toughness experiment demonstrated that the 1 hr UV exposure time on the boundary between the grains proved to be the strongest of the three experiments. The force-displacement curve exhibits several sudden drops in the load. The real time images are compared to various points on the force-displacement curve. Figure 3.6 shows the force-displacement curve and the points of load drops with the associated real time images displayed under the plot. When analyzing the data and images, locations P1 and P2 (“P” denoting *pre-crack*) show similar images in which material failure has not yet occurred. Just after failure occurs, the first load

drop, location A1 (“A” denoting *after-crack*), shows that a crack developed within the 10 hr grain. This is the highest irradiation and therefore the most brittle grain, used in the current grain pattern (Figure 2.3). When this crack reaches the more ductile boundary (which has been irradiated for only 1 hr), it arrests and the force-displacement curve levels off. After additional applied displacement (recall that the experiment is conducted in displacement control) another load drop occurs. This is associated with the formation of another crack developing in another 10 hr grain and is shown with location A2. The load continues to decrease and eventually these two cracks coalesce, extend, and then arrest at the next set of grain boundaries, resulting in the image shown for location A3. The last load drop is related to other crack developments in both a 5 hr and 10 hr grain that were a few seconds apart, and is denoted as location A4. The final order in which the cracks develop in this case is exhibited schematically in Figure 3.7, where the shaded blue circles with numbers display the order of crack occurrence. By comparing the force-displacement curve with acquired real time images, the load drops were associated with the developments of cracks within the material. Additionally, the high boundary toughness only produced cracks within the grains, *i.e., transgranular failure*. Note that all the cracks developed in this case are co-linear, indicating a 100 % transgranular crack growth. The main effect of the grain boundaries is to arrest cracks that have formed in the interior of the much weaker grains.

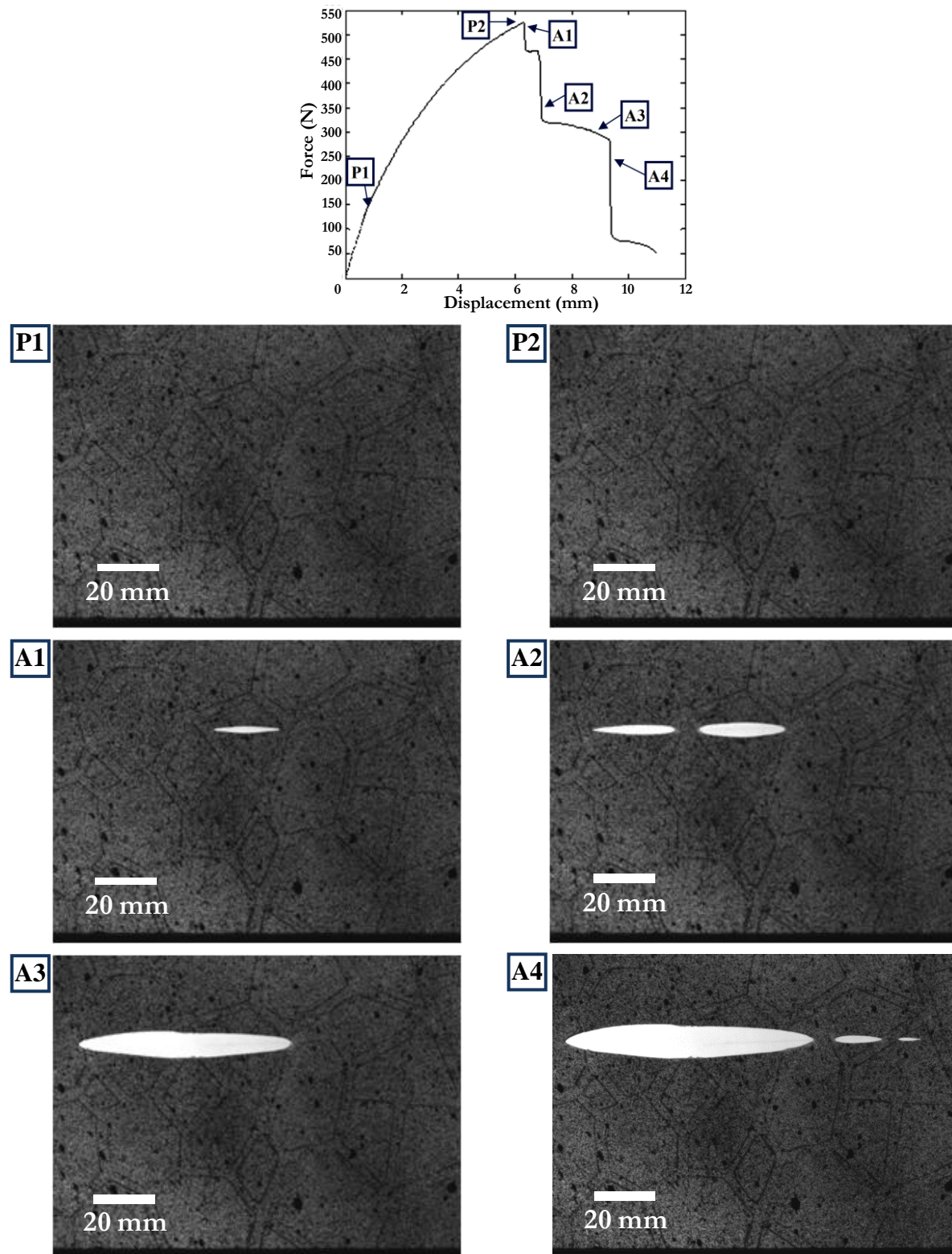


**Figure 3.6** Force-displacement response of the high boundary toughness specimen with blue boxed locations showing the real time images below the graph (pre failure denoted as P1 and P2, and additional locations after initial failure marked with A1, A2, *etc.*)

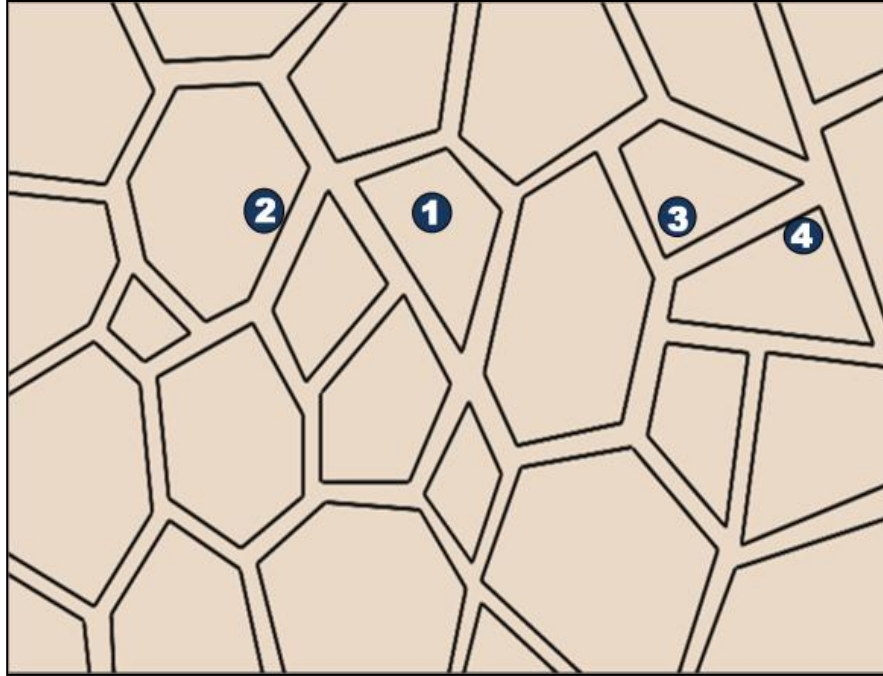


**Figure 3.7** Occurrence of cracks of the high boundary toughness in the order of which they appear throughout the test on an image of the granular template (order of crack occurrences marked with shaded blue circle).

### ***3.2.2 Medium Boundary Toughness - 10 Hr Irradiation***

The second set of granular samples were subjected to 10 hrs of UV exposure time on the boundary between the grains, thus embrittling the grain boundary region, and yielded a maximum force less than that of the high boundary toughness samples. In this case, the force-displacement curve (Figure 3.5) shows a different behavior compared to the high boundary toughness experiment, namely a more gradual decrease after the peak load rather than a sudden drop as was seen in the high boundary toughness results. Real time images were again taken during the experiment and selective images from different times were compared to the force-displacement curve. Figure 3.8 shows the force-displacement curve and the points of load drops with the associated real time images marked with numbers at the times when they were taken. As before, in images P1 and P2, early on in the loading and right before peak load, no failure is



observed; during this period it is seen that the force-displacement curve has a nonlinear behavior. Immediately following the peak load, it was observed that the crack developed *within the UV irradiated 10 hr boundary*. This crack is associated with the first load drop at location A1 of the force-displacement curve and its image, A1, is shown in Figure 3.8. This is in stark contrast with the previous case (the high boundary toughness) where failure initiated inside the grains. Seconds after the first crack developed, a second crack developed *within* a 10 hr irradiated grain and can be seen in image A1 in Figure 3.8 at the top left corner of the material. The remaining cracks that occurred for the medium toughness experiment are seen from locations at A2, A3, and A4 of the force-displacement curve. Analyzing the crack occurrences in sequence, it is apparent that there is a *competition* between the failure at the grain boundaries and within the grains themselves. The cracks form at different, and not coplanar, locations in the specimen either at the weakest boundaries or within the weakest grains (10 hrs). However, since both of the weakest grains and the grain boundaries have been irradiated by 10 hrs, they possess similar local properties. The force-displacement curve load drops are once again associated with crack development in either a boundary or a grain. The load drops, though, are much more gradual for the medium toughness experiments as the failure modes, *i.e., intergranular and transgranular*, compete with one another. The overall order of occurring cracks is displayed in Figure 3.9.

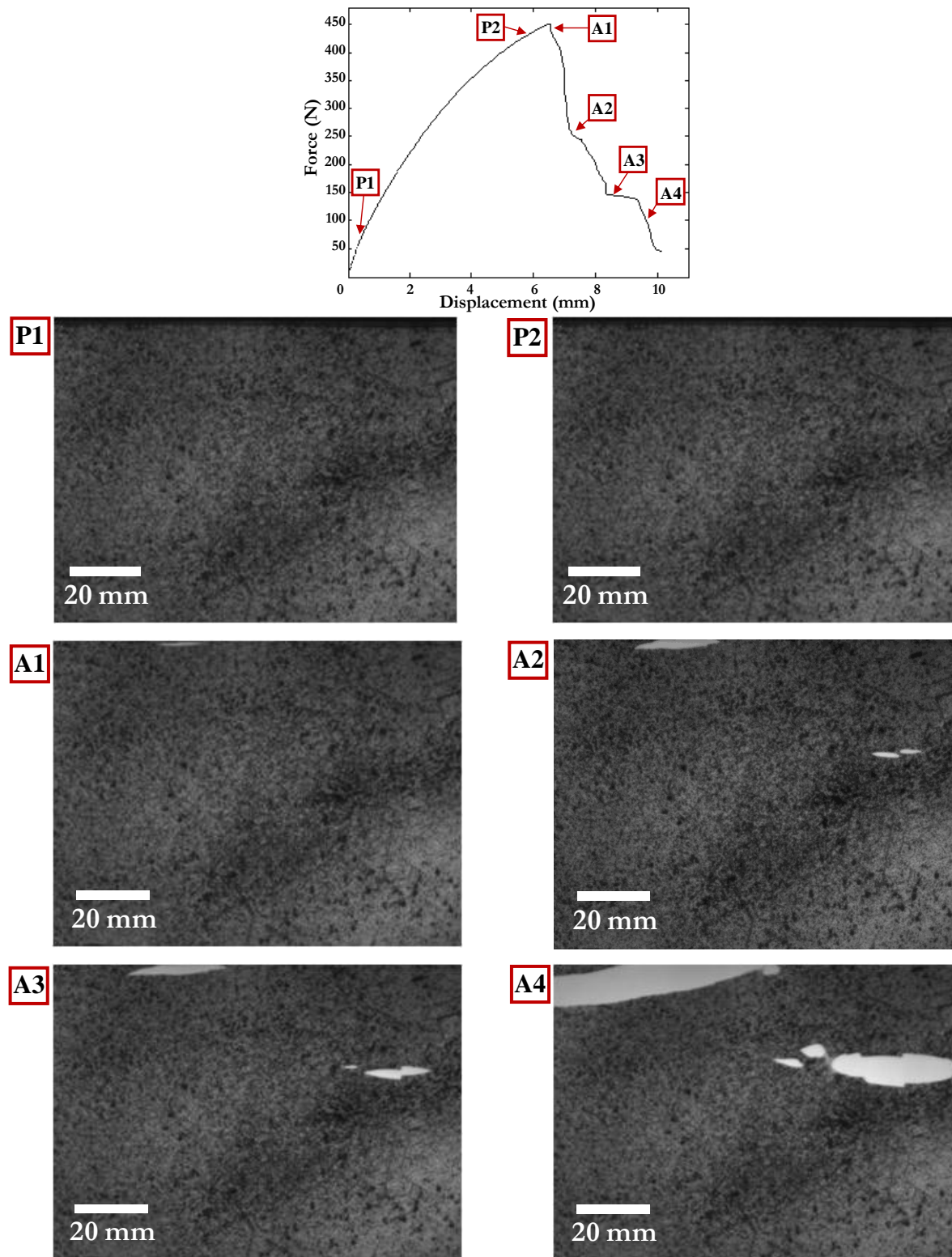


**Figure 3.8** Force-displacement response of the medium boundary toughness specimen with red boxed locations showing the real time images below the graph (pre failure denoted as P1 and P2, and additional locations after initial failure marked A1, A2, etc.)

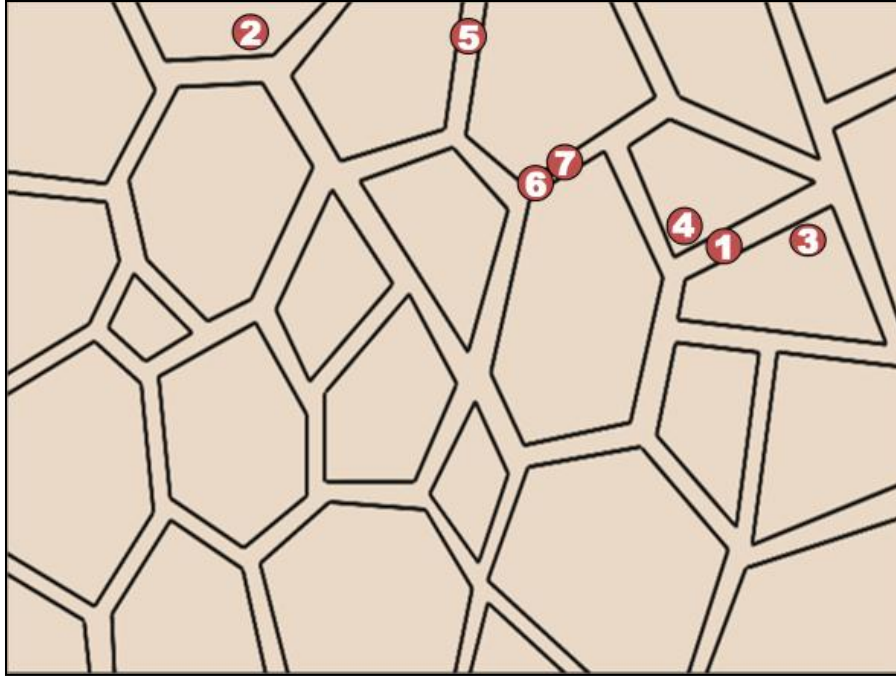


**Figure 3.9** Occurrence of cracks for the medium boundary toughness in the order of which they appear throughout the test on an image of the granular template (order of crack occurrences marked with shaded red circle).

### ***3.2.3 Low Boundary Toughness - 50 Hr Irradiation***

The last granular experiment was performed on a sample with 50 hrs of grain boundary irradiation, which considerably embrittles the grain boundaries compared to the interior of grains which have undergone at most up to 10 hrs of irradiation. The force-displacement curve for this case (Figure 3.10) again demonstrates nonlinear behavior from the beginning of the tensile loading, and no failure prior to peak load is visually observed (Figure 3.10 location P1). Note that the white spots visible near the top of the images in Figure 3.10 are a result of a poor speckle pattern and should not be mistaken for cracks. The first crack developed after 6.3 mm of displacement at a location on a 50 hr irradiated boundary denoted by A1 on force-displacement curve and real time image. At loads corresponding to the markers A2, A3, and A4 on the load-displacement curve, all of which are part of the gradual load drop, cracks developed within

seconds of each other starting first on a different 50 hr irradiated grain boundary, then within a 5 hr irradiated grain, and finally a 10 hr irradiated grain, respectively. The last crack developed within a 10 hr grain and is denoted by marker A5. With the increase in grain boundary UV exposure, and consequently grain boundary embrittlement, the competition between intergranular and transgranular failure modes becomes evident, and has tilted more in the favor of intergranular failure. In this case, the first two cracks that developed occurred on different grain boundaries. The remaining cracks then fail within the grains. Figure 3.11 shows the order of crack development throughout the duration of the low toughness experiment. Clearly as the load is in the vertical direction, even though locally stresses will be inhomogeneous because of the local grain property changes, it is difficult for the cracks to grow exactly along grain boundaries. However, it might be expected that if UV exposure of the grain boundaries were considerably increased, this would suppress any failure within the grains and would result in strictly intergranular failure. Nonetheless, even in this case the initiation of failure is clearly intergranular, unlike the earlier cases. Recall that in all samples the grain properties (both elasto-plastic and failure) were kept the same; it was only the grain boundary toughness that was tailored.

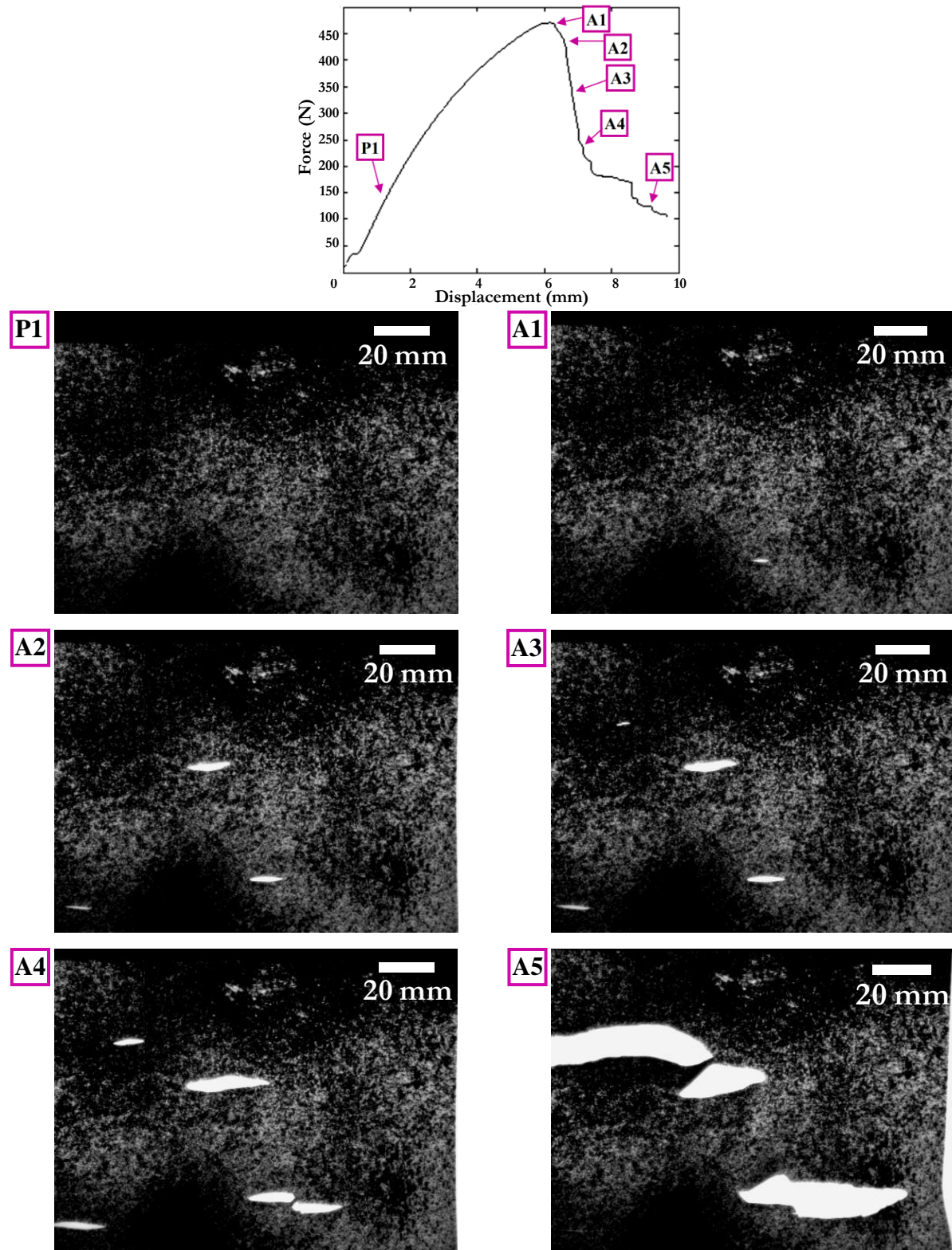


**Figure 3.10** Force-displacement response of the low boundary toughness specimen with magenta boxed locations showing the real time images below the graph (pre failure denoted as P1, and additional locations after initial failure marked A1, A2, *etc.*)



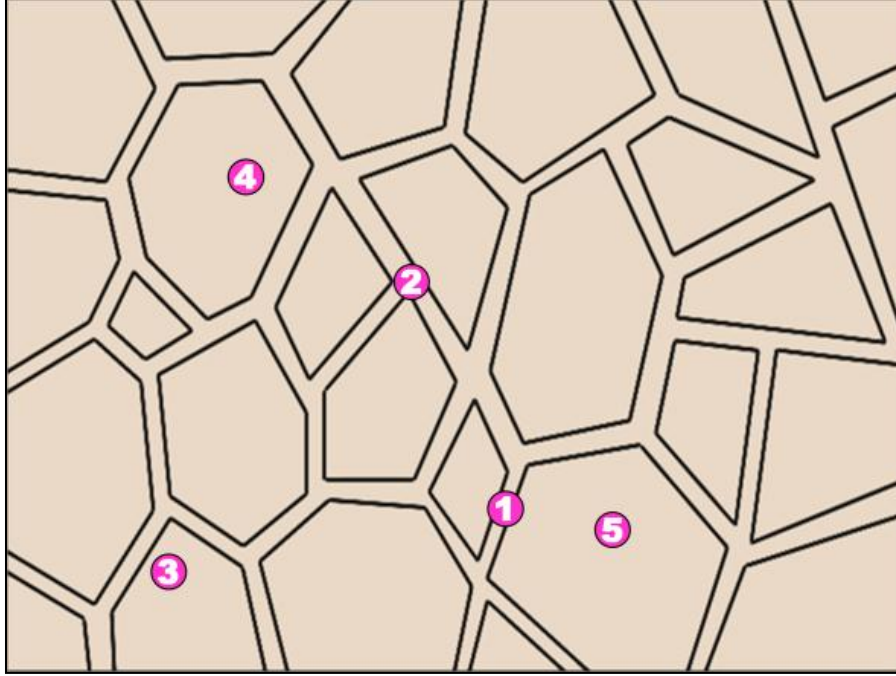


**Figure 3.11** Occurrence of cracks for the low boundary toughness specimen in the order of which they appear throughout the test on an image of the granular template (order of crack occurrences marked with shaded magenta circle).

### 3.3 Digital Image Correlation Results

In addition to visual information described above, we can quantitatively measure local strain inhomogeneities using the optical technique of DIC on the three different granular boundary toughness experiments. As described in Section 2.4, a reference image was taken prior to the start of each experiment, and subsequent images of the surface speckle pattern (examples of which were shown in Figures 3.6, 3.8, and 3.10) were captured in real time during each experiment. In the next section we will compare the DIC-measured strain fields along with the force-displacement curves. The strain field that is looked at in these particular results is the strain in the direction of the applied load, in the y-direction,  $\epsilon_{yy}$ . The importance of focusing on  $\epsilon_{yy}$  is due to the direction of the load that resulted from applying the material under tension and the

information obtained from this strain field. The shear strains,  $\varepsilon_{xy}$ , and the strains in the x-direction,  $\varepsilon_{xx}$ , were also measured using DIC but only selected images will be displayed for the high boundary toughness. The DIC results will help shed light on crack development and the strain fields prior to and after failure.

### ***3.3.1 High Boundary Toughness– 1 Hr Irradiation***

Prior to failure we expect inhomogeneous strain and stress fields to develop because of the tailored granular structure of the sample. This does indeed occur, even at fairly small loads in the high boundary toughness case. A selected sequence of DIC-measured  $\varepsilon_{yy}$  strains can be seen in Figure 3.12; they have been taken at applied displacements of (a) 1.57 mm, (b) 3.57 mm, (c) 5.57 mm, (d) 6.31 mm, (e) 6.79 mm, and (f) 6.90 mm. Note that after the last image shown in Figure 3.12(f), the DIC correlation fails because of the presence of multiple cracks with significant opening displacement. The DIC calculations following the high boundary toughness test begin from the end of the shifted data, which is shown as a dotted line. From this point, the strain field begins with the uniform strain of zero. As the displacement increases, the strain field develops inhomogeneously throughout the material. At 1.57 mm displacement, Figure 3.12(a) shows portions of the material reaching a strain of 1.25 %. Although the strain resolution is considerable, the strain localization does not specifically follow a particular grain boundary. As the displacement increases to 3.57 mm, a strain concentration begins to develop with a peak strain of 3.75 % near the middle right-hand side of the material as shown by Figure 3.12(b). The high strain region becomes more concentrated at 5.57 mm of applied displacement. Once the applied displacement reaches 6.31 mm, failure becomes visible and can be seen in Figure 3.12(d) as the secondary strain localization in the middle of the material. After the crack develops, a

strain field typical of a central crack is visible as depicted in Figure 3.12(e) (Anderson, 1995). Because there is a high strain concentration at the crack tip, the field region surrounding this concentration are overwhelmed by it, and thus it affects further failure directly coplanar with the original crack. Figure 3.12(f) displays this occurrence of the formation of another crack due to the high strain concentration from an existing crack.

The interesting result of this experiment demonstrates the fact that failure can occur outside a region of high strain concentration. In a homogeneous material, the material would fail at the point the strain is highest. Due to the local inhomogeneities of this material with the varying UV exposure times, failure can indeed occur in areas of lower strain as indicated in Figure 3.12(d).



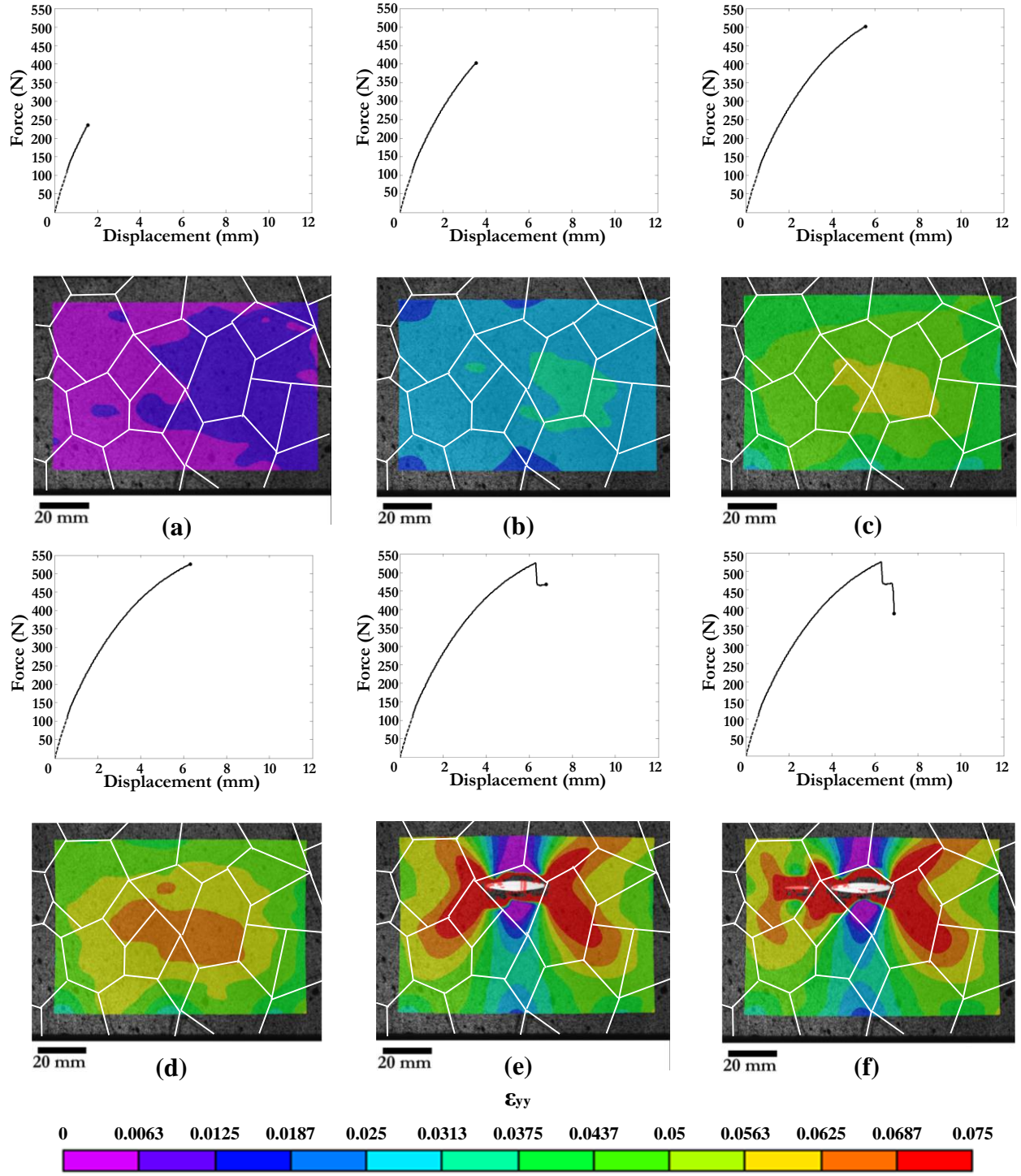


**Figure 3.12** Force-displacement response of the high boundary toughness specimen in relation to DIC strain measurements,  $\epsilon_{yy}$ , for displacements of: (a) 1.57 mm (b) 3.57 mm (c) 5.57 mm (d) 6.31 mm (e) 6.79 mm (f) 6.90 mm.

As mentioned earlier, the shear strains and x-directional strains were also measured using DIC. Figure 3.13 shows two examples of strain fields with their respective strain measurements. The pictures in this figure are taken at the peak load where crack development begins. Figure 3.13(a) and (b) shows the same exact time as in Figure 3.12(d) with a far field displacement of 6.31 mm. Figure 3.13(a) shows the shear strain,  $\epsilon_{xy}$ , and Figure 3.13(b) shows the x-directional strain,  $\epsilon_{xx}$ . When analyzing these figures, the existence of an inhomogeneous field is present, but the figures do not give much information regarding strain concentration and crack initiation as the results in Figure 3.12. Therefore, the  $\epsilon_{yy}$  field will only be shown for the remaining sections.

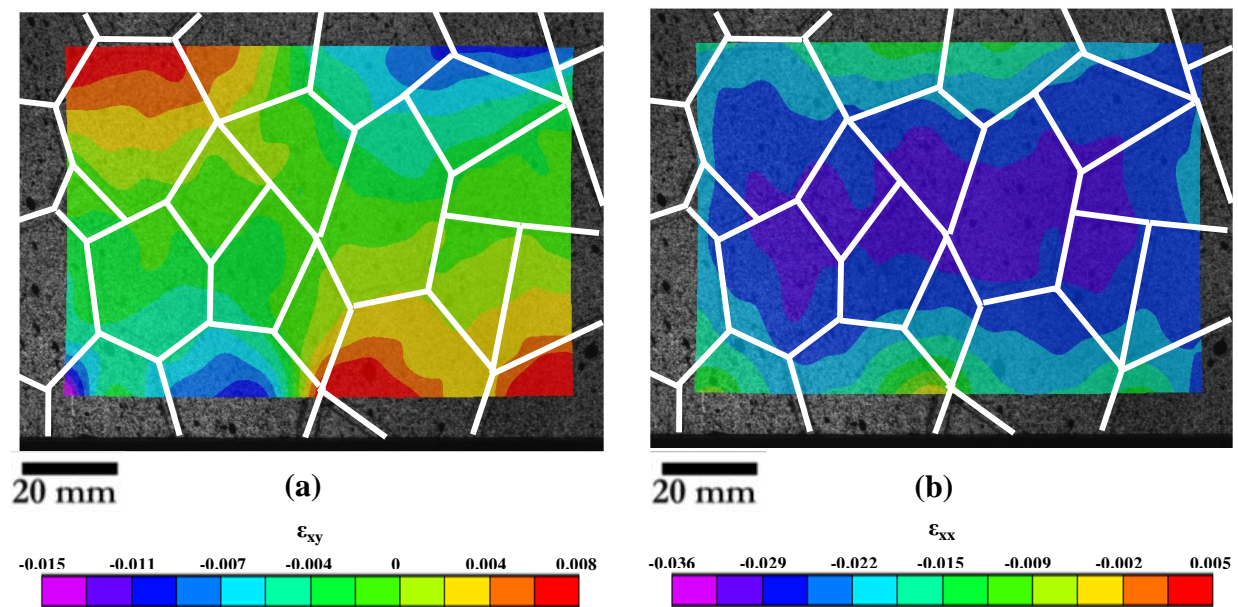


**Figure 3.13** DIC measurements of (a) the shear strain,  $\epsilon_{xy}$ , and the (b) x-direction strain,  $\epsilon_{xx}$ , at crack initiation with 6.31 mm of displacement.

### ***3.3.2 Medium Boundary Toughness – 10 Hr Irradiation***

Throughout the duration of the medium boundary toughness experiment, the strain fields show a more noticeable inhomogeneous behavior that better follows the grain boundary structure than previous experiments. Strain fields that display significant strain localizations are shown in Figure 3.14 at applied displacements of (a) 1.31 mm, (b) 4.31 mm, (c) 6.53 mm, (d) 6.87 mm, (e) 7.58 mm, and (f) 9.31 mm. At 1.31 mm displacement, Figure 3.14(a) displays varying regions of the material reaching strains up to 1.16 %. An increase of displacement to 4.31 mm places the material under varying strains ranging from 1.16 % to 3.5 % (Figure 3.14(b)). At the peak load and displacement of 6.53 mm, Figure 3.14(c) does not detect high strains near the region of failure, but shows strain localization around the middle left region of the material with a peak strain of 5.83 %. It is not until the load drops and the material has undergone a displacement of 6.87 mm that failure is detected by DIC. At this point, Figure 3.14(d) shows the appearance of three cracks with strain concentrations visibly surrounding the crack tips. One of the cracks appears in the upper portion of the material within a 10 hr irradiated grain. This crack was near the outer range of the real time image window, and DIC could not correlate the result for this crack because the speckles moved out of the field of view in comparison to the reference image. This behavior demonstrates that failure can occur outside a region of high strain concentration depending on the local properties. Figures 3.14(e) and (f) illustrate strain fields surrounding the cracks, including the crack outside of the DIC field of view. The high strain concentrations surrounding the crack tips overwhelm the surrounding areas and formations of new cracks appear. Figure 3.14(f) demonstrates this observation as three cracks develop one after another in a row due to the strain concentrations that develop from previous cracks.

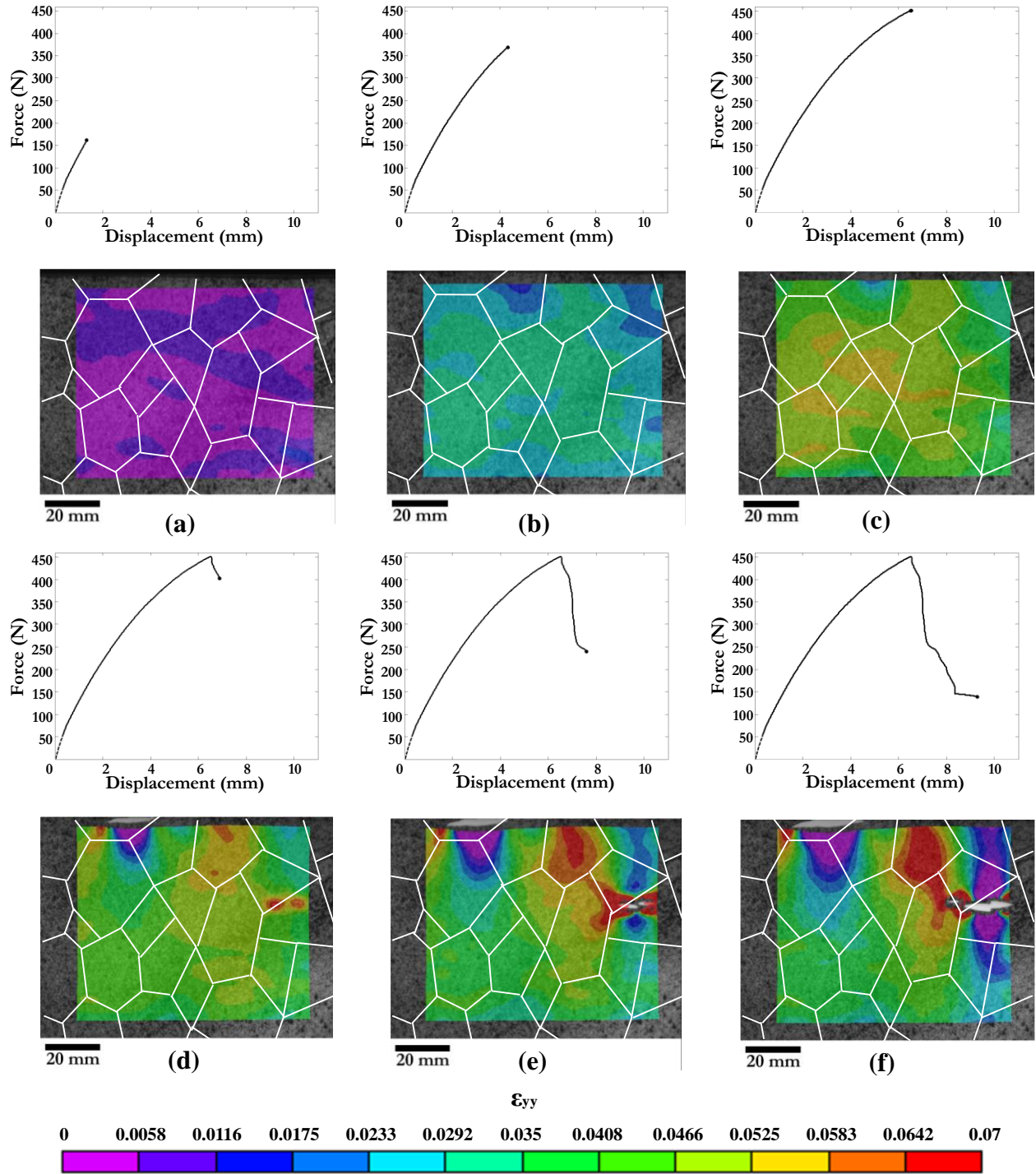


**Figure 3.14** Force-displacement response of the medium boundary toughness specimen in relation to DIC strain measurements,  $\epsilon_{yy}$ , for displacements of: (a) 1.31 mm (b) 4.31 mm (c) 6.53 mm (d) 6.87 mm (e) 7.58 mm (f) 9.31 mm.

### ***3.3.3 Low Boundary Toughness – 50 Hr Irradiation***

For the low boundary toughness experiment, the strain fields again show inhomogeneous behavior as expected. Strain fields that display a significant behavior of strain localization are shown in Figure 3.15 and include displacements of (a) 3.1 mm, (b) 5.1 mm, (c) 6.1 mm, (d) 6.6 mm, (e) 6.9 mm, and (f) 7.1 mm. As the displacement increases to 3.1 mm, Figure 3.15(a) displays a small region of the material reaching strains up to 3.5 %. Figure 3.15(b) shows the material with an increase to 5.1 mm of displacement and this causes the low boundary toughness specimen to undergo varying strains ranging from 3.5 % to 6.42 % (Figure 3.15(b)). At the peak load and displacement of 6.1 mm, Figure 3.15(c) shows the DIC detection of high strains near the region of failure and shows strain localization surrounding it, with strains between 5.83% and 7%. In this specific experiment, failure occurred within the region of high strain concentration as depicted in Figure 3.15(b) with the peak strain of 6.42 %. The formation of two cracks occurred at a displacement of 6.6 mm and shows peak strains up to 7 % as displayed in Figure 3.15(d). High strain concentration from these cracks lead to the development of additional failures that occur within areas aware of such crack tip concentrations. Figures 3.15(e) and (f) show the development of multiple cracks within these areas of high strain concentrations up to 7 %. In the low boundary toughness experiment, a magnitude of failures developed within the material and the initial failure occurred within the high strain concentration region prior to crack visibility.



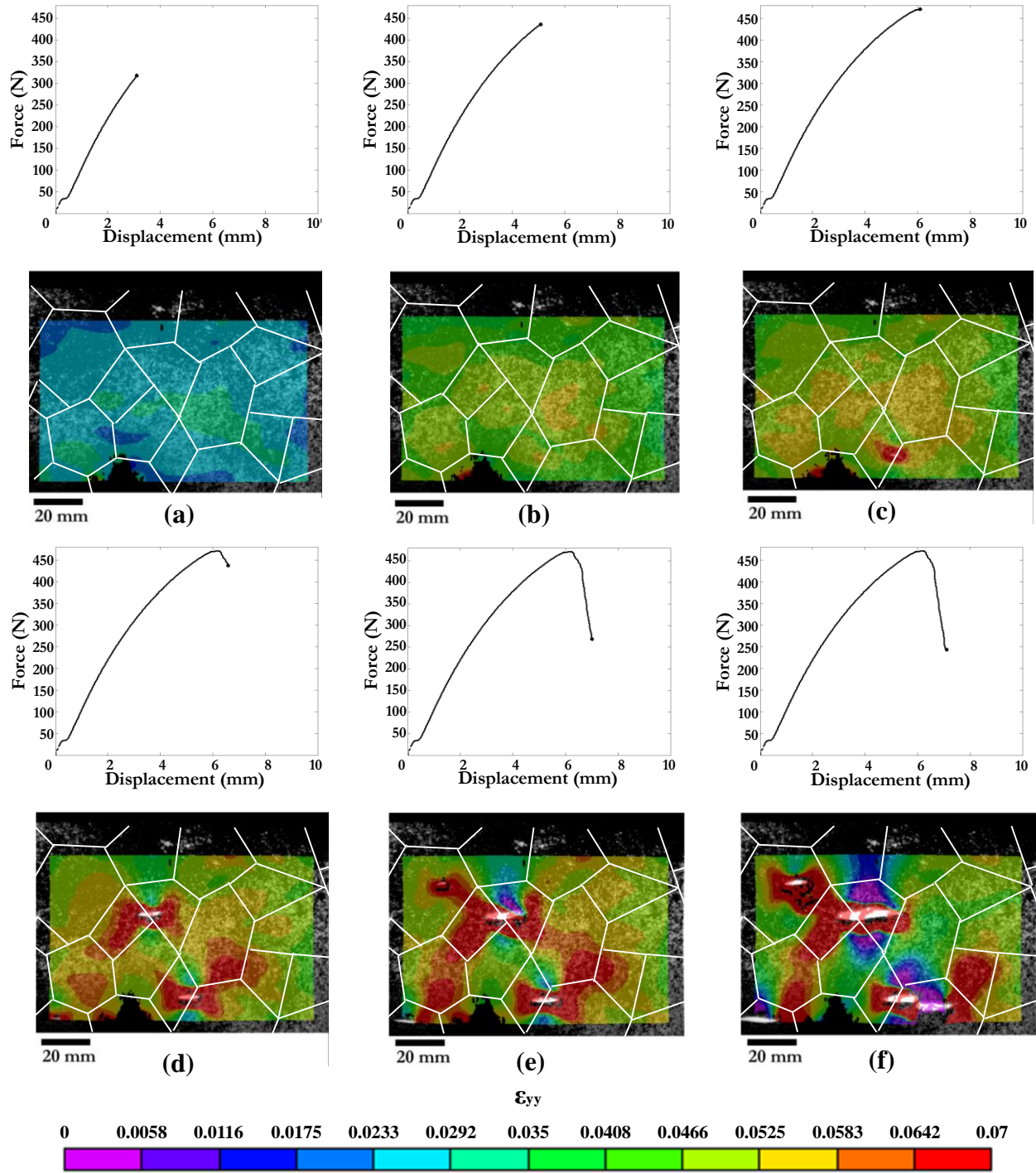


**Figure 3.15** Force-displacement response of the low boundary toughness specimen in relation to DIC strain measurements,  $\epsilon_{yy}$ , for displacements of: (a) 3.1 mm (b) 5.1 mm (c) 6.1 mm (d) 6.6 mm (e) 6.9 mm (f) 7.1 mm.

## Chapter 4

### Finite Element Analysis

#### 4.1 Numerical Setup

##### 4.1.1 Interface and Interphase Models

In order to assist with the overall study of the inhomogeneous granular specimen, numerical models were created using the finite element program, ABAQUS 6.10. The numerical development first began with the creation of a model database, followed by a model of the geometry consisting of a rectangle with dimensions of 100 mm  $\times$  150 mm, *i.e., the dimensions of the actual ECO granular specimen excluding the grip areas.*

Two different designs were used, the interface and the interphase models. The granular templates following the actual arrangement used in the experiments were sketched onto the rectangular geometry (using the partition function while in sketch mode) for both models. The *interphase model*, which can be seen in Figure 4.1 with a mesh pattern superposed on it (see Section 4.1.4), approximates the experimental granular specimen a bit more closely. This is because, in addition to separate grains of different irradiation time, it allows for finite areas around the grain boundaries to have distinct properties of their own. The width of these grain boundaries in the experiments were typically around 3 mm; however, because of the likelihood of UV light scattering around the edges of the template used for irradiation, the interphase boundary region will be larger than the nominal 3 mm. Thus the boundary width will become a parameter that will be varied to investigate what effect it will have on the resulting specimen response. For a benchmark comparison we will also consider the case of zero grain boundary thickness, what we term the *interface model*, which is seen in Figure 4.2, accounts for different

grain irradiation only. In both cases the numerical results obtained will not account for material failure, but the interface model will be able to account for the mechanical effects introduced by the differing elasto-plastic properties of the boundary interface region.

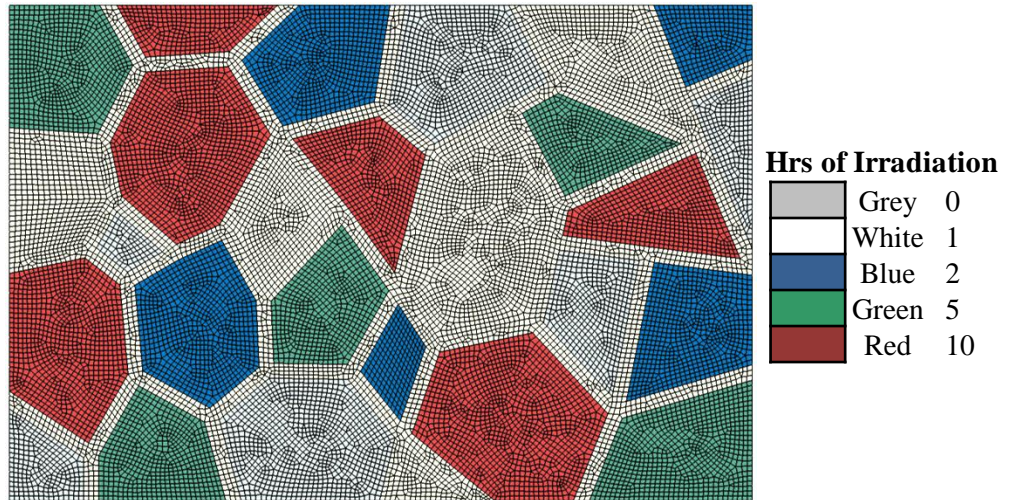


**Figure 4.1** Interphase model used for finite element simulations. In this model, the grain boundaries show irradiation of 1 hr. Color key for each irradiation time can be seen to the right.

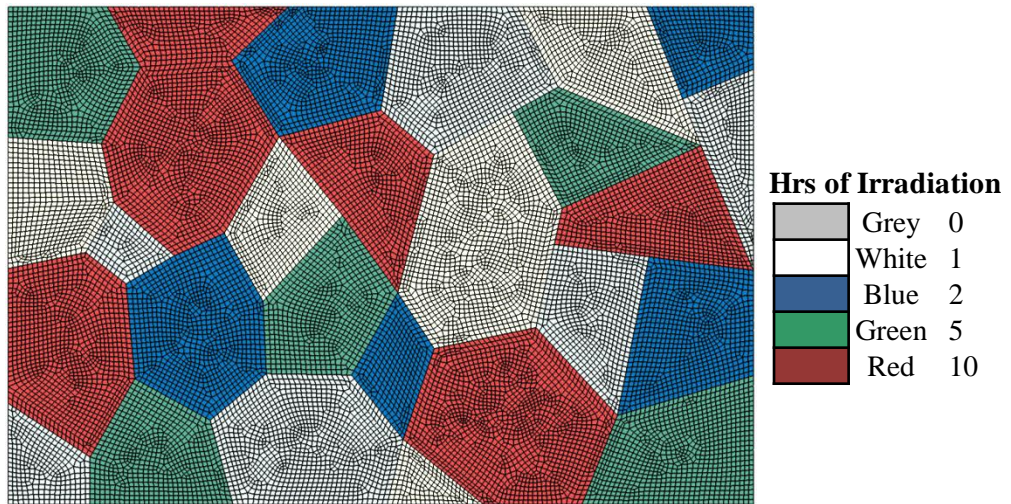


**Figure 4.2** Interface model used for simulation. In this model, the grain boundaries are excluded. The color key for the rest of the grains can be seen to the right.



#### 4.1.2 Material Property Allocation

After the geometric design of the numerical model, the material properties were defined and assigned to the different grains and boundaries. The property module within ABAQUS was used to define properties of varying mechanical response corresponding to different UV irradiations. Various sections were then created by assigning the material properties to a particular geometry of the model using the experimental configurations described in Section 2.2.2. Five different material models were created corresponding to 0 hr, 1 hr, 2 hr, 5 hr, and 10 hr irradiation. The properties used in the model were obtained from the typical stress-strain curves of each of these hours of irradiation as measured experimentally (Figure 3.1), *i.e.*, the *nominal stress-strain curves*. In order for ABAQUS to interpret the data correctly, the true stress and strain values were calculated. The true strain was calculated by converting the experimental strain data to the true strain using:

$$\varepsilon^{total} = \varepsilon = \ln(1 + \varepsilon_{nom}) \quad (4.1)$$

where  $\ln$  is the natural log function,  $\varepsilon$  is the true strain, or total strain, and  $\varepsilon_{nom}$  is the nominal strain. The true stress,  $\sigma$ , was calculated by:

$$\sigma = \sigma_{nom}(1 + \varepsilon_{nom}) \quad (4.2)$$

where  $\sigma_{nom}$  is the nominal stress and  $\varepsilon_{nom}$  is the nominal strain, which were acquired from experiments. Both the elastic and plastic properties were defined in separate inputs within the property module. For the elastic portion, the required properties were the material's Young's modulus and the Poisson's ratio. The Young's modulus was calculated using the elastic portion

of the stress-strain curves. The Poisson's ratio was taken to be  $\nu = 0.45$  based on Abanto-Bueno and Lambros, (2004). For the plastic portion, the yield stress and corresponding plastic strain (beginning from zero plastic strain) were input in a tabular fashion. The plastic strain,  $\varepsilon^{pl}$ , was calculated using:

$$\varepsilon^{pl} = \varepsilon^{total} - \varepsilon^{el} = \varepsilon^{total} - \frac{\sigma_y}{E} \quad (4.3)$$

where  $\varepsilon^{total}$  is the total strain calculated from equation 4.1 and  $\varepsilon^{el}$  is the elastic strain calculated using equation 4.2 but using the true yield stress,  $\sigma_y$ , divided by the material Young's modulus,  $E$ . Table 4.1 shows the Young's modulus for the varying materials as well as the true yield stress. Based on the tabulated values of the uniaxial plastic stress strain law, ABAQUS employs a  $J_2$  theory. ABAQUS uses this  $J_2$  deformation theory of plasticity with a power law hardening material (Ramberg-Osgood) for the model of the experimental data of plastic strain that was provided. Yield is assumed to occur based on the von Mises yield criterion. In all cases small strain theory was assumed to apply even though the strains in the material can become very large. This strain behavior tends to happen towards the end of the experiments after failure has occurred, which is a regime not investigated in this numerical analysis. Furthermore, all experimental data of stress strain curves have been obtained assuming small strains.

**Table 4.1** Young's modulus and true yield stress values for different hours of irradiation used for numerical properties

Varying UV Exposures (Hrs)	Young's Modulus (MPa)	True Yield Stress (MPa)
0	150.38	3.875
1	157.12	2.392
2	160.93	1.824
5	172.55	1.925
10	189.85	2.107

Different material properties are assigned to the different sections within the granular medium as described above. By assigning sections, each of which is individually defined as a solid and homogeneous, plane stress conditions are assumed, since our sample thickness is small. The nominal sheet thickness is taken as 0.48 mm, but in our measurement it actually varies from 0.48 mm to 0.51 mm. In fact, it is often somewhat difficult to accurately measure the thickness since the compliance of ECO produces an underestimate of the thickness if too much force is applied on the micrometer used to make the measurement. Therefore, in the numerical simulations the thickness will also be parametrically varied from 0.48 mm to 0.51 mm.

#### ***4.1.3 Boundary Conditions***

The next step in the analysis consisted of defining the appropriate boundary conditions to simulate the experimental set-up. The loading in the experiments was conducted under displacement control conditions at a rate of 0.5 mm/min. As the material is very compliant with respect to the load frame, it is assumed that the entire displacement occurs at the gauge section. In addition, since the rate is very slow, even compared to the wave speeds in this compliant polymer (Abanto-Bueno and Lambros, 2004), quasi-static loading is assumed in the simulations. Therefore, in order to simulate this loading, the entire bottom edge of the model was held fixed in the vertical direction, *i.e.*,  $u_y = 0$ . Additionally, in order to fix the model in space, the bottom left corner was set not to move in the horizontal direction as well, *i.e.*,  $u_x(0,0) = 0$ . Because the experimental SENT tests involved displacement control, the displacement in the y-direction was defined for each simulation for displacements up to 6.3 mm (the average displacement right before failure). In this fashion, since displacement is applied to the model, the resulting load can be monitored and can be considered an output of the simulation, and it can be compared to the

load measured experimentally. Figure 4.3 schematically illustrates the boundary conditions applied to the numerical model.

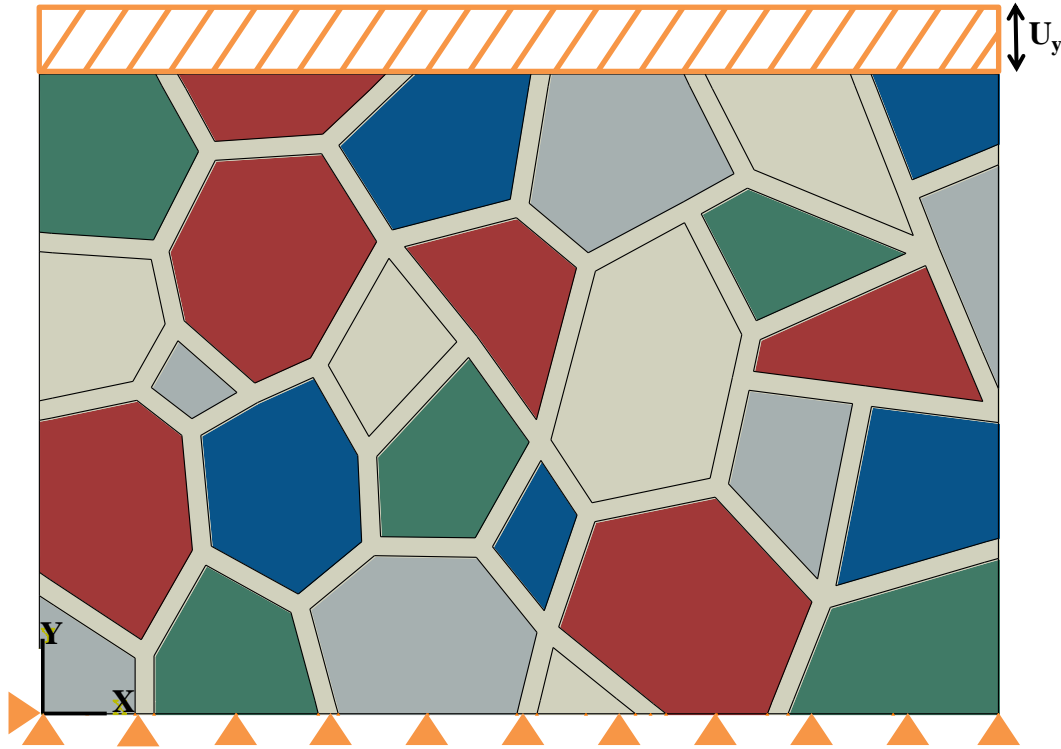


**Figure 4.3** Interphase model showing applied boundary conditions. The entire bottom edge has  $u_y = 0$ ; the bottom left corner also has  $u_x = 0$ , and the entire top edge a  $u_y$  specified displacement (in mm) as recorded from the experiments.

#### 4.1.4 Mesh

The last step in carrying out the numerical simulation was defining the mesh on the model. The entire sample was meshed since there is no symmetry in this problem. Because the accuracy of the results depends on the meshing of the assembly, several mesh refinement tests were done to ensure that the final mesh employed had results that were converged. Quadratic elements were used for all test meshes, and each had an average nodal distance of 6 mm (Figure 4.5(a)), 5 mm (Figure 4.5(b)), 4 mm (Figure 4.5(c)), 3 mm (Figure 4.5(d)), 2 mm (Figure 4.5(e)),

and 1 mm (Figure 4.5(f)). Depending on the location, the nodal distance can increase or decrease in order to fit the geometry properly; a nodal distance greater than 7 mm would cause the simulation to fail due to the large elements.

Two methods of evaluating mesh convergence were used, one global and one local. Globally, the load output from the simulations was used to compare with experimentally measured values. Therefore we investigated whether this load had converged while refining the mesh. In addition, the local stress distribution was also used as a measure of convergence with mesh refinement. The reaction force values for varying meshes were taken at all the top edge nodes individually and then summed to get the total force applied for a given applied distance. For all of the different meshes used, the force-displacement curves appear identical from afar, as can be seen in Figure 4.4. Zooming into the curves in Figure 4.4 shows that the meshes with average nodes of 1 mm, 1.3 mm, and 1.5 mm converge. Due to the convergence of the different mesh sizes, there is great confidence toward the force-displacement curves developed for each simulation (interphase and interface).

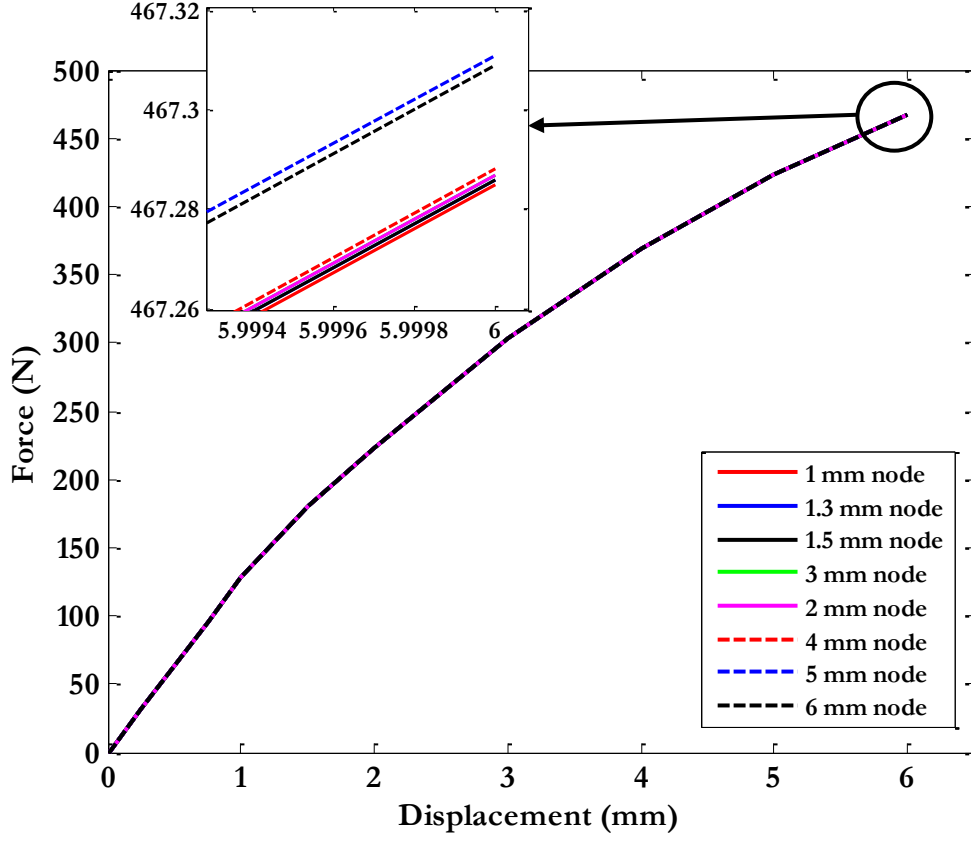


**Figure 4.4** Mesh convergence for varying average nodal displacements for interphase model.

The second mesh convergence test that was used involved comparing the stresses in the y-direction,  $\sigma_{22}$ , for each mesh. The stress fields were compared for 6 mm of applied displacement, *i.e., well along the load-displacement curve but before initial failure*, and contours of  $\sigma_{22}$  can be seen in Figure 4.5. In contrast to the load-displacement curves where convergence occurred from 1.5 mm of average nodal distances, when looking at Figures 4.5(a)-(f), we see that the stress field is not clearly defined for the coarser meshes. As the nodal distances decrease, the stress fields take on a more defined shape. Figures 4.5(e) and (f) show mesh convergence as the stress fields are nearly identical. Therefore the mesh that was used for the remainder of the numerical simulations was the 1 mm nodal distanced mesh, corresponding to the stress state in

Figure 4.5(f), which produced 19,003 elements within the model. Figures 4.5(a)-(e) produced 1,016; 1,243; 1,758; 2,661; and 4,799 elements respectively.

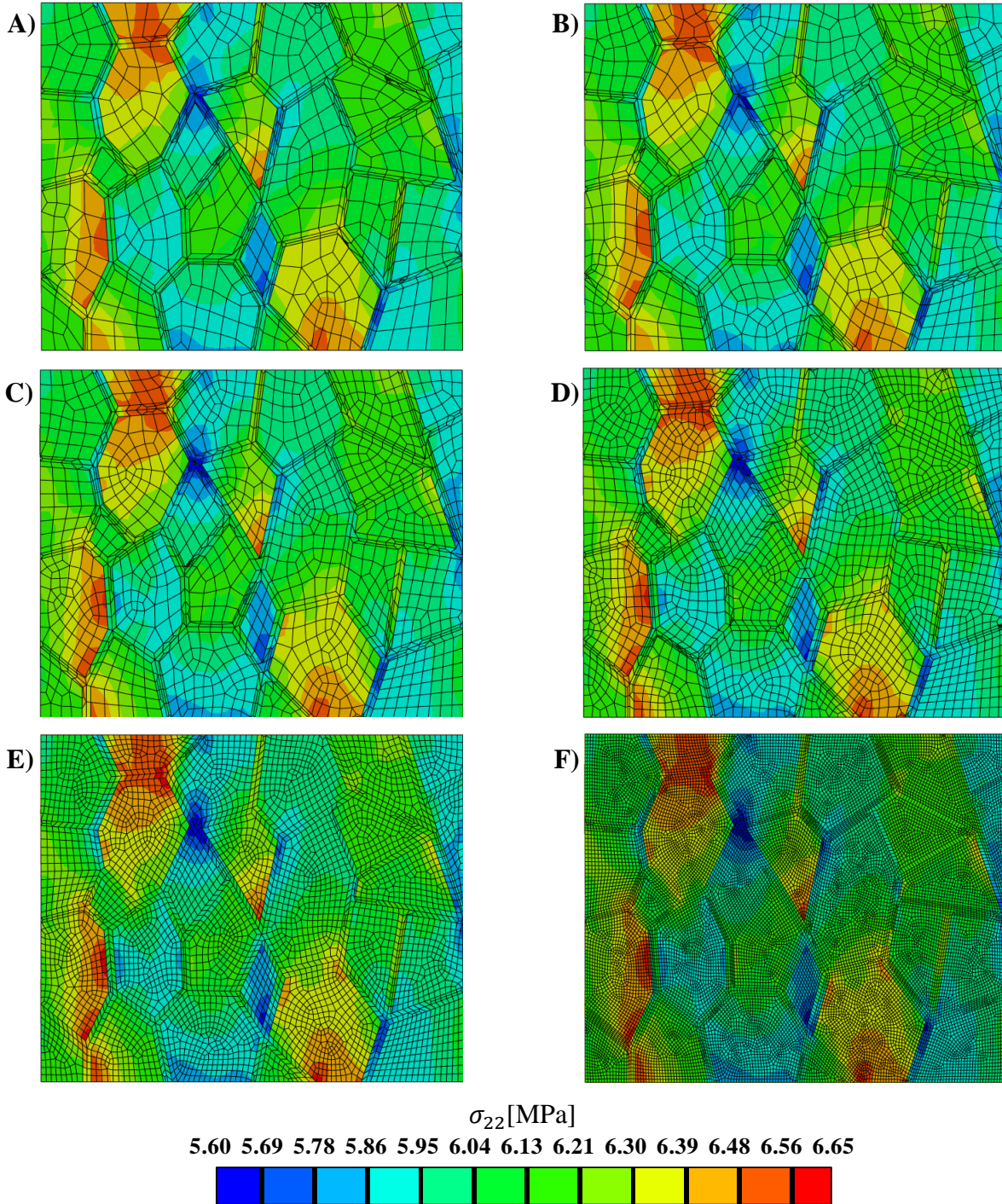


**Figure 4.5** Numerically simulated stress fields produced for 6 mm of displacement for varying meshes of different nodal distances: (a) 6 mm, (b) 5 mm, (c) 4 mm, (d) 3 mm, (e) 2 mm, and (f) 1 mm. These images were used as a mesh convergence test to choose which mesh to implement.

## 4.2 Numerical Results

Numerical simulations were performed for both the interface and interphase cases. For the interphase model, only boundary irradiations of 1 hr (high boundary toughness, Section 3.2.1) and 10 hr (medium boundary toughness, Section 3.2.2) were considered. The low and high range of the material thickness measured was used in simulation (*i.e.*, 0.48 mm and 0.51 mm) and the boundary width was varied from 3 mm to 6 mm, since as explained earlier it will in general be larger than the 3 mm gap used in the mask to make the samples. The following sections present the numerical simulation results in comparison to the experimental results.

### 4.2.1 Interface Model

The first numerical simulation was the interface model which essentially neglects the influence of the grain boundary thickness in the development of the stress field. The simulation was performed for a displacement of 6 mm (displacement prior to failure). Note that in this case there is one curve for all experiments since the grain irradiation pattern is the same in all cases and we are ignoring any boundary thickness effects for the numerical interface model. The simulated force-displacement curve was plotted against the experimentally recorded one for the high, medium, and low boundary toughness specimens. Figure 4.6 shows the numerical interface model results, dashed green line, for a specimen thickness of 0.51 mm. Although the interface model agrees well with the low boundary toughness case, the comparison with the high and medium boundary toughness experiments is not as good. In order to distinguish between different boundary irradiations (since our model does not incorporate failure simulation), we use an interphase model.



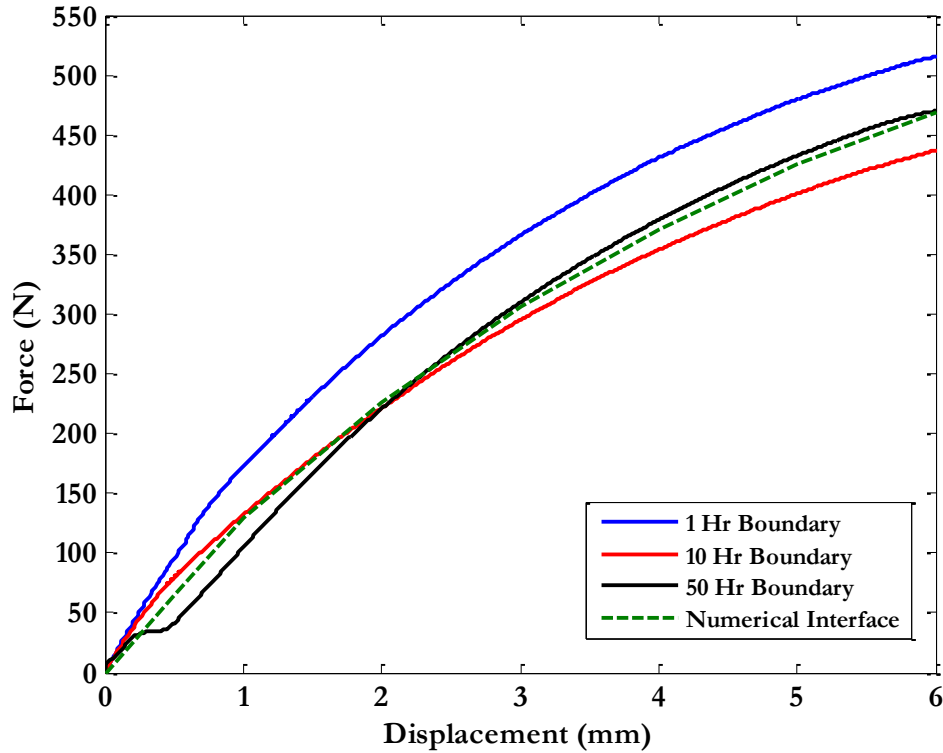


**Figure 4.6** Interface model with a thickness of 0.51 mm plotted against actual experiments.

#### **4.2.2 Interphase Model - High Boundary Toughness**

For the high boundary toughness model, four different cases were simulated that used the low and high range values of the material thickness (0.48 mm and 0.51 mm) and of the boundary widths (3 mm and 6 mm). The results of the four different simulations can be seen in Figure 4.7 along with the corresponding experimental curve. The sensitivity of the results to the boundary width is small compared to the sensitivity to the sample thickness. As the sample thickness increases, the simulation results approach closer to the experimental values, although generally it is as accurate as the interface model shown earlier. It is worth remembering that between 0 and 5 hrs of irradiation there is significant material variability in ECO properties (Figures 3.2-3.4).

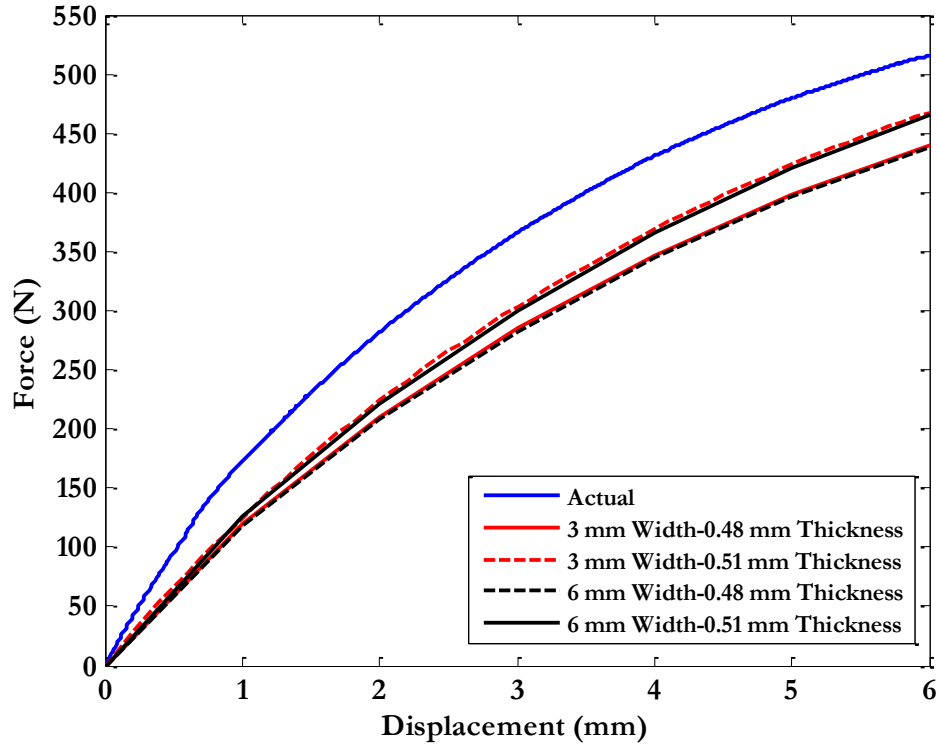


**Figure 4.7** Interphase high boundary toughness simulations compared to actual. Simulation included low and high range of the material thickness (0.48 mm and 0.51 mm) and the boundary widths of 3 mm and 6 mm.

Since the force-displacement curve increases with increasing thickness, the material thickness in the simulations was increased further to determine if a particular thickness value would better represent the experimental results. This parametric behavior on sample thickness can be seen in Figure 4.8. As the thickness increases, the force increases but none of the plotted results adequately capture the beginning of the experimental force-displacement curve, although at later stages the results from the 0.58 mm sample thickness agrees with the experimental results. In this model, the curve that had the best identical behavior was the 0.58 mm thickness with 3 mm boundary width.

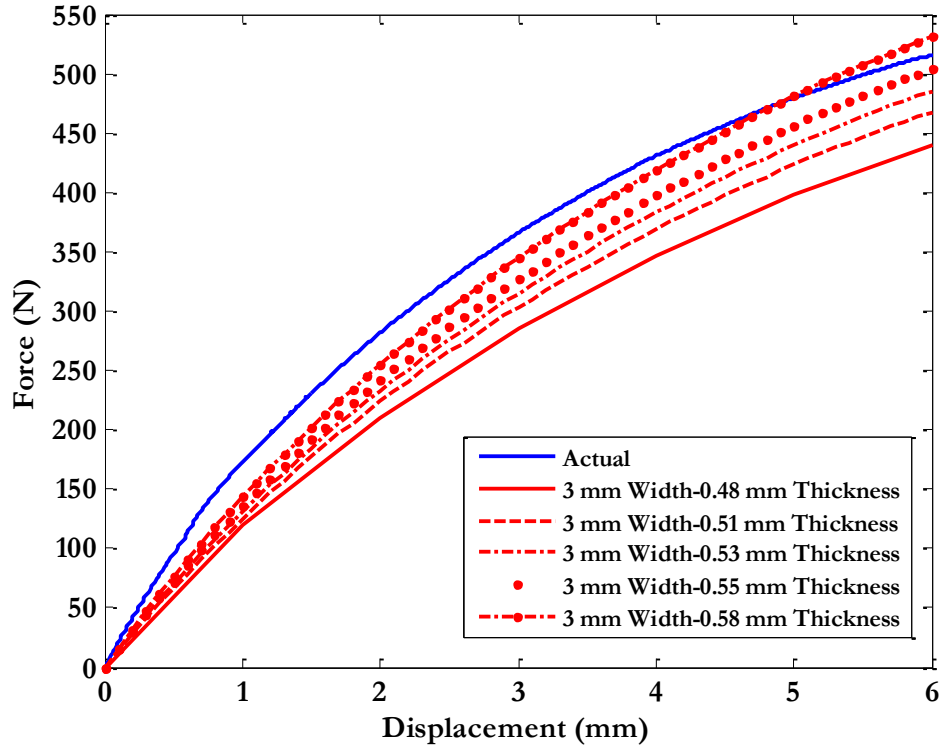


**Figure 4.8** Interphase high boundary toughness simulations with increasing thickness compared to actual.

#### 4.2.3 Interphase Model - Medium Boundary Toughness

For the medium boundary toughness model, the same four cases were simulated, *i.e.*, the low and high range values of the material thickness (0.48 mm and 0.51 mm) and of the boundary widths (3 mm and 6 mm). The results of the four different simulations as well as the corresponding experimental measurements can be seen in the force-displacement plots of Figure 4.9. The simulation results from using a sample thickness of 0.48 mm and boundary width of 3 mm (black line) compared the best to the actual experiment. From the results in the medium and high boundary toughness model, the variations in the boundary width did not play a significant role in the model but it is clear that material thickness indeed plays a great role in trying to simulate the experimental results.

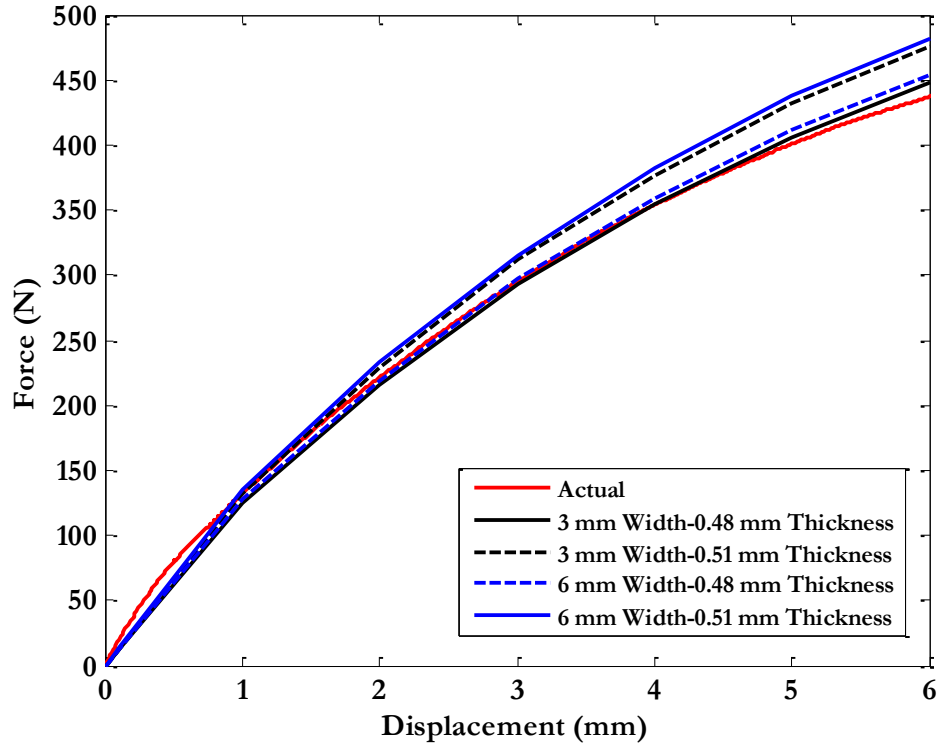


**Figure 4.9** Interphase medium boundary toughness simulation compared to actual. Simulation included low and high range of the material thickness (0.48 mm and 0.51 mm) and the boundary widths of 3 mm and 6 mm.

### 4.3 Failure Criteria

After comparing the experimental and numerical force-displacement data which showed similarities, we attempt to determine in the models where failure, *i.e.*, *crack initiation*, would occur. We will use the standard, for metallic materials, yields criteria of von Mises or Tresca to access failure initiation. An applied displacement value of 6.3 mm was used for the simulation which was the common experimentally recorded displacement value immediately prior to failure development, *i.e.*, *when the initial drop in the load was recorded*. From the simulations, the von Mises, or the equivalent stress, and the maximum shear stress were obtained.

As discussed in chapter 3, the high boundary toughness experiment developed the first two cracks *inside* 10 hr irradiated grains followed by crack initiation in a 5 hr and then another

10 hr irradiated grain. The sequence can be seen in the schematic microstructure of Figure 4.10(a) which shows the sequence of crack development. The von Mises stress obtained from simulation corresponding to this experiment, presented in Figure 4.10(b), shows stress concentrations in several areas but all within grains of the material. Three of the highest concentrations are seen in the three grains that had cracks occur within them in the experiment. In contrast with the maximum shear stress (Figure 4.10(c)), it is apparent that there is a high concentration within the 10 hr irradiated grain in which failure first developed. However with both failure criteria the general areas of failure development can be predicted. However, we do not at this stage have a one-to-one correspondence between the magnitude of the critical values of boundary strength and the von Mises or Tresca failure parameters. It may be possible to extend this failure prediction further by adding a cohesive-type failure response (Kandula *et. al.*, 2006) to the grain boundary region that would draw the cohesive properties from the *a priori* known mechanical characterization of the grain boundaries.

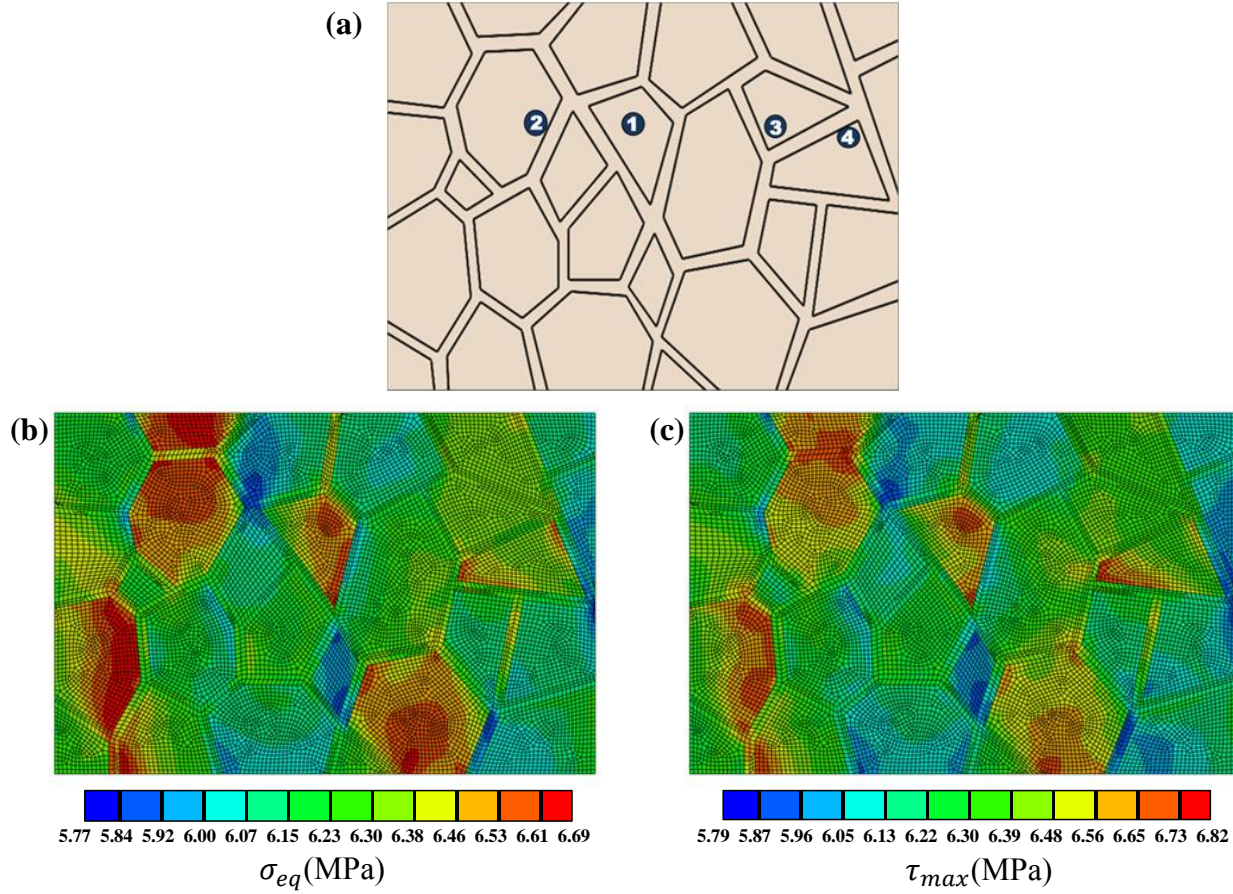


**Figure 4.10** a) The order of crack initiation, shown by numbers, for the high boundary toughness experiment; b) Von Mises yield criterion displaying areas of high equivalent stress; c) Tresca max shear stress yield criterion displaying areas of high max stress.

The medium boundary toughness experiment first developed cracks within the 10 hr boundary *and* grain just seconds after one another (Figure 4.11(a)). The remaining cracks initiated within the boundaries and grains. Looking at the results for the equivalent stress at the instant of failure initiation in Figure 4.11(b), we see concentrations within grains as well as boundaries – in contrast with the results for the previous experiment. The 10 hr grain and boundary in which the first two cracks develop clearly show high stress concentrations. The maximum shear stress shows similar behavior, but also shows concentrations at the location of the first two crack occurrences as well as other more defined areas (Figure 4.11(c)). It is a bit more difficult to tell where crack development will occur as large areas of the grain boundaries



show high yield concentrations as well as some grains themselves. However, the analysis does confirm the fact that there is a competition between intergranular and transgranular failure. In addition, in Figures 4.11(a) the formation of “force chains” becomes evident. These are collections of grains that because of their alignment to the loading direction (or in this case their local properties) are more favorably inclined to carry more stress than their neighbors (but may have more or less strain than their neighbors depending on their local constitutive response). Series of grains roughly aligned in the vertical direction act synergistically to carry larger amounts of the applied load. Such force chains are visible in Figure 4.11(a) as the vertical areas of high stress concentration.

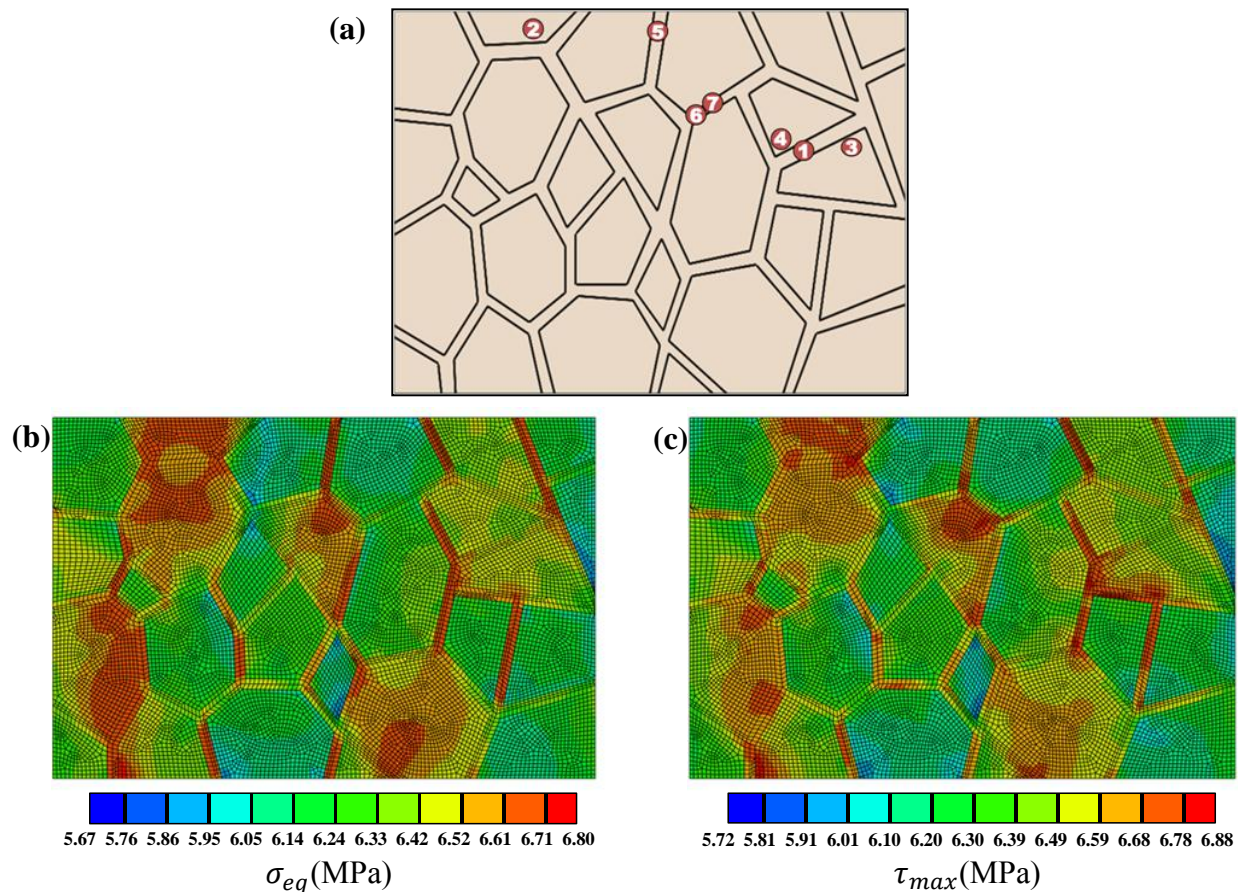


**Figure 4.11** a) The order of crack initiation, shown by numbers, for the medium boundary toughness experiment; b) Von Mises yield criterion displaying areas of high equivalent stress; c) Tresca max shear stress yield criterion displaying areas of high max stress.

## **Chapter 5**

### **Conclusions and Future Work**

The main objectives of this work were to study the mechanical response of well controlled microstructures, tailor the model material, ECO, to create different failure modes, and use numerical models to validate the experimental results. Knowledge of the local grain and grain boundary properties led to additional studies towards different arrangements that can experimentally help study crack path selection problems. The results obtained in this work illustrate, at the macroscale and the microscale, the influence of local microstructures in relation to the development of strain fields, while bypassing the issue of through-thickness effects by using very thin samples.

Given the variability of the material, ECO, uniaxial tension tests were carried out for different irradiation times in order to assess the effects of UV exposure on the mechanical properties of our particular batch of ECO. In previous works (Abanto-Bueno and Lambros, 2004), it was seen that with increasing irradiation time, the elastic modulus increases, the failure stress increases, and failure strain decreases, thus effectively embrittling the material.

Exploiting the tailorability of ECO based on UV exposure time allowed for the development of a granular pattern with controllable grain and grain boundary elasto-plastic and failure properties. The specimen design included grains and grain boundaries similar to the microstructure of a metal and worked as a puzzle in which all the individual grains and the boundary pieces could be placed on top of an ECO sheet during irradiation. For a given grain structure, UV exposure on the grain boundaries was for 1 hr, 10 hr, and 50 hr. Knowledge of the local properties, and the assumption that the UV irradiation is uniform throughout the material,



addressed the issues raised in the introduction regarding the combined use of DIC and EBSD techniques in previous studies (Zhang and Tong, 2004; Matin *et. al.*, 2006; St-Pierre *et. al.*, 2008; Hatamleh *et. al.*, 2009; Carroll *et. al.*, 2010; Rehr *et. al.*, 2011).

In the case of the 1 hr grain boundary irradiation, *i.e.*, *high boundary toughness*, the DIC results demonstrate the fact that, depending on local toughness, failure can occur outside a region of high strain concentration. In a homogeneous material, the material would fail at the location where the strain/stress is the highest. Because of the local (tailored) inhomogeneities of this material, failure occurred in areas of lower strain – in this particular case only with grains. It is notable that the high boundary toughness *only* produced cracks within the grains, *i.e.*, *failure was solely transgranular*, and produced rapid drops in the far field load. Also, all cracks developed in this case are collinear, denoting a 100% transgranular crack growth.

For the 10 hr grain boundary irradiation, *i.e.*, *medium boundary toughness*, the behavior of this experiment contrasts greatly with the high boundary toughness since failure initiated *inside* the grains. For medium boundary toughness, there is competition between the failure at the grain boundaries (intergranular) and within the grains themselves (transgranular), which causes the macroscale load drops to be much more gradual than the case of high boundary toughness. The material behavior in this experiment again demonstrates that failure can occur outside a region of high strain concentration depending on the local properties.

The 50 hr grain boundary irradiation experiment, *i.e.*, *low boundary toughness*, illustrated that the increase in irradiation considerably embrittled the grain boundaries compared to the grain interior which underwent a (local) maximum of only 10 hr of irradiation. With this increased brittleness, intergranular failure becomes more pronounced, although the competition between the two failure modes persists. The first two cracks that developed in this case occurred

on a grain boundary, so failure initiation was intergranular, as expected. However, as these initial cracks arrested because of constraints by the surrounding material, the remaining cracks formed in grain interiors, making the rest of the failure event transgranular. It is expected that any further increase in UV exposure time of the grain boundary regions results in increased amounts of intergranular failure – perhaps exclusively so for large irradiation times. However, because of the length of time involved in specimen preparation, this notion was not pursued in this study.

Numerical analysis of two different models, *interface* and *interphase*, while varying settings of boundary widths and material thickness enabled the development of models that closely represent the experimental results. The macroscale force-displacement curves shown in the interface model resulted in a well-served representation of the low boundary toughness specimen. However, the interface model did not compare well to the high and medium boundary toughness experiments, as it does not include the presence of the boundaries themselves; therefore, the interphase model was used to simulate the two remaining cases. For the high boundary toughness experiment, the interphase model for a 0.58 mm thickness sample with a 3mm boundary region width showed similar behavior to the actual force recorded. The medium boundary interphase model for the same parameters showed the best comparison to the actual experiment. The von Mises and Tresca failure criteria that were applied to the simulation results produced good agreement with the observed failure initiation sites. Although a polymeric material was used here, each criterion showed high magnitudes of stress near the areas where failure occurred in the experiments.

The results produced from this study have provided an increased knowledge of the effects of UV exposure on ECO. The tailored pattern of the microstructure of a metal served as a starting point for the granular specimens developed in this work, and in tailoring the grain and

grain boundary structure to understand failure mode competition and to control crack path development, a significant amount of information was gathered. Additionally, the finite element simulations yielded promising results that validated the experimental aspects of this study.

Regarding future efforts, additional experimental and numerical work is needed to further confirm the findings related to transgranular and intergranular failure. Specific to the experimental aspect, higher irradiation experiments will help confirm failure modes and gain additional understanding of the manner in which failure develops. Using higher irradiation exposure times than the lower exposure times used in this study will help towards the development of controlled crack path materials. Regarding future numerical work, additional models need to be developed utilizing higher exposure times and different patterns. Following the simulations of such models, experimental testing can help validate such numerical results and potential failure prediction. In order to predict material failure, a cohesive failure model can be used to simulate fracture in ECO based from the work of Kandula *et. al* (2006). As mentioned in Section 4.4, a cohesive-type failure response can be added to the grain boundary region that would draw the cohesive properties from the *a priori* known mechanical characterization of the grain boundaries. Following the determined cohesive properties, a finite element work can be used to implement a cohesive model to help predict crack initiation and propagation (Kandula *et. al.*, 2006).

## References

- Abanto-Bueno J., Lambros J., “Mechanical and Fracture Behavior of an Artificially UV-Irradiated Poly(ethylene-carbon monoxide) Copolymer”, *Journal of Applied Polymer Science*, Vol. 92, pp.139-148 (2004).
- Anderson T.L., “Fracture Mechanics: Fundamentals and Applications”, 2nd ed., (1995).
- Andrady A.L., “Weathering of Polyethylene (LPDE) and Enhanced Photodegradable Polyethylene in the Marine Environment”, *Journal of Applied Polymer Science*, Vol. 39, No. 2, pp. 363-370 (1990).
- Andrady A.L., Pegram J.E., and Nakatsuka S., “Studies on Enhanced Degradable Plastics: The Geographic Variability in Outdoor Lifetimes of Enhanced Photodegradable Polyethylenes”, *Journal of Environmental Polymer Degradation*, Vol. 1, No. 1, pp. 31-43 (1993).
- Andrady A.L., Pegram J.E., and Searle N.D., “Wavelength Sensitivity of Enhanced Photodegradable Polyethylenes, ECO, and LDPE/MX”, *Journal of Applied Polymer Science*, Vol. 62, No. 9, pp. 1457-1463 (1996).
- Bartali A. E., Aubin V., Degallaix S., “Surface Observation and Measurement Techniques to Study the Fatigue Damage Micromechanisms in a Duplex Stainless Steel”, *International Journal of Fatigue*, v. 31, p. 2049 (2009).
- Carroll J., Efstathiou C., Lambros J., Sehitoglu H., Hauber R., and Spottswood S., “Investigation of Fatigue Crack Closure using Multiscale Image Correlation Experiments”, *Eng Fract Mech.*, 76, pp. 2384–2398 (2009).
- Carroll J., Abuzaid W., Lambros J., and Sehitoglu H., “An Experimental Methodology to Relate Local Strain to Microstructural Texture”, *Review of Scientific Instruments*, v. 81, article 083703 (2010).
- Chu T.C., Ranson W.F., Sutton M.A., and Peters W.H., “Applications of Digital-Image Correlation Techniques to Experimental Mechanics”, *Experimental Mechanics*, Vol. 25, No. 3, pp. 232-245 (1985).
- Efstathiou C., Sehitoglu H., and Lambros J., “Multiscale Strain Measurements of Plastically Deforming Polycrystalline Titanium: Role of Deformation Heterogeneities”, *International Journal of Plasticity*, Vol. 26, pp. 93–106 (2010).
- Field D.P., Magid K.R., Mastorakos I.N., Florando J.N., Lassila D.H., Morris J.W. Jr., “Mesoscale Strain Measurement in Deformed Crystals: A Comparison of X-Ray Microdiffraction with Electron Backscatter Diffraction”, *Philosophical Magazine*, v. 90, p. 1451 (2010).

- Furneaux, G.C., Ledbury, K.J., and Davis, A., "Photo-Oxidation of Thick Polymer Samples-Part I: The Variation of Photo-Oxidation with Depth in Naturally and Artificially Weathered Low Density Polyethylene", *Polymer Degradation & Stability*, Vol. 3, No. 6, pp. 431-442 (1981).
- Gerday A.F., Bettaieb M. Ben, Duchêne L., Clement N., Diarra H., Habraken A.M., "Material Behavior of the Hexagonal Alpha Phase of a Titanium Alloy Identified from Nanoindentation tests", *European Journal of Mech.*, Vol. 30, Issue 3, , Pages 248-255 (2011).
- Hartley G.H. and Guillet J.E., "Photochemistry of Ketone Polymers. I. Studies of Ethylene-Carbon Monoxide Copolymers", *Macromolecules*, Vol. 1, No. 2, pp.165-170 (1968).
- Hatamleh O., Mishra R.S., Oliveras O., "Peening Effects on Mechanical Properties in Friction Stir Welded AA 2195 at Elevated and Cryogenic Temperatures", *Materials & Amp; Design*, Volume 30, Issue 8, Pages 3165-3173 (2009).
- Heskins M. and Guillet J.E., "Photochemistry of Ketone Polymers. III. Energy Transfer in Ethylene-Carbon Monoxide Polymers", *Macromolecules*, Vol. 3, No. 2, pp. 224-231 (1970).
- Hoffman M.J., Hammer M., Endriss A., Lupascu D.C., "Correlation between Microstructure, Strain Behavior, and Acoustic Emission of Soft PZT Ceramics", *Acta Materialia*, pp. 49:1301–10 (2001).
- Ivanova E., Chudnovsky A., Wu S., Sehanobish K., Bosnyak C.P., and Wu S., "A New Experimental Technique for Modeling of a Micro-Heterogeneous Media", *Experimental Techniques*, Vol. 20, No. 6, pp. 11-13 (1996).
- Kandula S.S.V., Abanto-Bueno J., Lambros J., and Geubelle P., "Cohesive Modeling of Quasi-Static Fracture in Functionally Graded Materials", *Appl. Mech.* 73, 783 (2006).
- Lambros J., Santare M.H., Li H., and Sapna III G.H., "A Novel Technique for the Fabrication of Laboratory Scale Model Functionally Graded Materials", *Experimental Mechanics*, Vol. 39, No. 3, pp. 184-190 (1999).
- Li S.K.L. and Guillet J.E., "Photochemistry of Ketone Polymers. XIV. Studies of Ethylene Copolymers", *Journal of Polymer Science: Polymer Chemistry Edition*, Vol. 18, pp. 2221-2238 (1980).
- Li R., Wu S., Ivanova E., Chudnovsky, Sehanobish K., and Bosnyak C.P., "Finite Element Method and Experimental Analysis of Crack-Inclusion Interaction", *Journal of Applied Polymer Science*, Vol. 50, No. 7, pp. 1233-1238 (1993).
- Li H., Lambros J., Cheeseman B.A., and Santare M.H., "Experimental Investigation of the Quasi-static Fracture of Functionally Graded Materials", *Journal of Solids and Structures*, Vol. 37, pp. 3715-3732 (2000).

- Lian J., Wang J., Kim Y.-Y., and Greer J., “Sample Boundary Effect in Nanoindentation of Nano and Microscale Surface Structures”, *Journal of the Mechanics and Physics of Solids*, Vol. 57 (5), pp. 812-827 (2009).
- Liu Y., Wang B., Yoshino M., Roy S., Lu H., and Komanduri R., “Combined Numerical Simulation and Nanoindentation for Determining Mechanical Properties of Single Crystal Copper at Mesoscale”, *J. Mech. Phys. Solids*, 53, pp. 2718–2741 (2005).
- Liu Y., Varghese S., Ma J., Yoshino M., Lu H., and Komanduri R., “Orientation Effects in Nanoindentation of Single Crystal Copper”, *Intl. J. Plasticity*, 24:1990–2015 (2008).
- Matin M.A., Vellinga W.P., Geers M.G.D., “Microstructure Evolution in a Pb-free Solder Alloy during Mechanical Fatigue”, *Materials Science and Engineering: A*, Volume 431, Issues 1-2, 15 September, Pages 166-174 (2006).
- Nakatsuka S. and Andrady A., “Studies on Enhanced Degradable Plastics. III. The Effect of Weathering of Polyethylene and (Ethylene-Carbon Monoxide) Copolymers on Moisture and Carbon Dioxide Permeability”, *Journal of Environmental Polymer Degradation*, Vol. 2, No. 2, pp. 161-167 (1994).
- Peters V.H. and Ranson V.F., “Digital Imaging Techniques in Experimental Stress Analysis”, *Optical Engineering*, Vol.21, No. 3, pp. 427-431 (1982).
- Peters W.H., Ranson W.F., Sutton M.A., Chu T.C., and Anderson J., “Application of Digital Correlation Methods to Rigid Body Mechancis”, *Optical Engineering*, Vol. 22, No. 6, pp. 738-742 (1983).
- Pierre St-L., Héripré E., Dexet M., Crépin J., Bertolino G., and Bilger N., “3D Simulations of Microstructure and Comparison with Experimental Microstructure coming from O.I.M Analysis”, *International Journal of Plasticity*, Vol. 24, pp. 1516–1532 (2008).
- Raabe D., Sachtleber M., Zhao Z., Roters F., Zaefferer S., “Micromechanical and Macromechanical Effects in Grain Scale Polycrystal Plasticity Experimentation and Simulation.” *Acta Materialia*, v. 49, p. 3433 (2001).
- Rehrl C., Kleber S., Antretter T., Pippan R., “A Methodology to Study Crystal Plasticity Inside a Compression Test Sample Based on Image Correlation and EBSD”, *Materials Characterization*, Vol. 62, pp. 793-800 (2011).
- Saai A., Louche H., Tabourot L., and Chang H.J., “Experimental and Numerical Study of the Thermo-Mechanical Behavior of Al bi-crystal in Tension using Full Field Measurements and Micromechanical Modeling. *Mech. Mater.*, Vol. 42, pp. 275–292 (2010).
- Sutton M.A., Wolters W.J., Peters W.H., Ranson W.F., and McNeill S.R., “Determination of Displacements Using an Improved Digital Image Correlation Method”, *Image and Vision Computing*, Vol. 1, No. 3, pp. 133-139 (1983).

- Torikai A., Takeuchi A., Nagaya S., and Fueki K., "Photodegradation of Polyethylene: Effect of Crosslinking on the Oxygenated Products and Mechanical Properties", *Polymer Photochemistry*, Vol. 7, No. 3, pp. 199-211 (1986).
- Trozzolo A.M. and Winslow F.H., "A Mechanism for the Oxidative Photodegradation of Polyethylene", *Macromolecules*, Vol. 1, No. 1, pp. 98-100 (1968).
- Zhang N. and Tong W., "An Experimental Study on Grain Deformation and Interactions in an Al-0.5% Mg Multicrystal", *International Journal of Plasticity*, v. 20, p. 523 (2004).